Final authors version - Accepted in Geochimica et Cosmochimica Acta -3rd September 2019

New constraints from Central Chile on the origins of enriched continental compositions in thick-crusted arc magmas

Penny E. Wieser[1,2*], Stephen J. Turner[3], Tamsin A. Mather[1], David M. Pyle[1], Ivan P. Savov[4] and Gabriel Orozco[5]

[1] Department of Earth Sciences, University of Oxford, South Parks Road, Oxford OX1 3AN, UK

[2] Now at Department of Earth Sciences, University of Cambridge, Downing Street, Cambridge, CB2 3EQ, UK.

[3] Washington University in St. Louis, One Brookings Drive, St. Louis, MO 63130, USA.

[4] School of Earth and Environment, Institute of Geophysics & Tectonics, University of Leeds, Leeds LS2 9JT, UK.

[5] Red Nacional de Vigilancia Volcánica, Servicio Nacional de Geología y Minería, Av. Santa María 0104, Providencia, Chile.

* Corresponding author: pew26@cam.ac.uk. Phone: 07593670818

Abstract

Magmas from continental arcs built on thick crust have elevated incompatible element abundances and "enriched" radiogenic isotope ratios compared to magmas erupted in island and continental arcs overlying thinner crust. The relative influence of the slab, mantle, and upper plate on this variability is heavily debated. The Andean Southern Volcanic Zone (SVZ; 33-46° S) is an ideal setting to investigate the production of enriched continental arc compositions, because both crustal thickness and magma chemistry vary coherently along strike. However, the scarcity of primitive magmas in the thick-crusted northern SVZ has hindered previous regional studies. To better address the origin of enriched continental compositions, we investigate the geochemistry (major and trace element abundances, $^{87}Sr/^{86}Sr$ and $^{143}Nd/^{144}Nd$ ratios) of new mafic samples from Don Casimiro and Maipo volcanoes in Diamante-Maipo Caldera Complex of the northern SVZ. While evolved Diamante-Maipo samples show evidence for crustal assimilation, the trace element and isotopic enrichment of the most mafic samples cannot result from crustal processing, as no known regional or global basement lithologies are enriched in all of the necessary incompatible trace elements. Subduction erosion models similarly fail to account for the enriched isotopic and trace element signature of these samples. Instead, we suggest that the enrichment of northern SVZ magmas is derived from an enriched ambient mantle component (similar to EM1-type ocean island basalts), superimposed on a northward decline in melt extent. A substantial, but nearly uniform contribution of melts from subducting sediment and altered oceanic crust are required at all latitudes. The EM1-like enrichment may arise from recycling of metasomatized subcontinental lithospheric mantle (M-SCLM), as the isotopic trajectory of primitive rear-arc monogenetic cones trend towards the compositions of SCLM melts sampled across South America. Isotopic

data from spatially distributed rear-arc centres demonstrate that the arc-parallel variations in the degree of EM1-type enrichment observed in arc-front samples are also present up to 600 km behind the trench in the rear-arc. Rear-arc trace element systematics require significant but variable quantities of slab melts to be transported to the mantle wedge at these large trench distances. Overall, we show that a unified model incorporating variable mantle enrichment, slab additions, and melt extents can account for along and across-arc trends within the SVZ. The recognition that mantle enrichment plays a key role in the production of enriched continental compositions in the SVZ has important implications for our understanding of the chemical evolution of the Earth. If ambient mantle enrichment is not taken into account, petrogenetic models of evolved lavas may overestimate the role of crustal assimilation, which, in turn, may lead models of continental crust growth to overestimate the amount of continental material that has been recycled back into the mantle.

Key Words

- Mantle heterogeneity
- Andean Southern Volcanic Zone
- EM1
- Sub continental lithospheric mantle

1. Introduction

Magmas which erupt from continental arc-front stratovolcanoes are compositionally distinct from oceanic arc magmas. With the exception of volcanics from intra-arc rift zones (e.g., Conrey et al., 2004), continental magmas exhibit elevated incompatible element abundances, steeper incompatible trace element patterns (Fig. 1a), and often have isotopic signatures offset to higher $^{87}Sr/^{86}Sr$ and lower $^{143}Nd/^{144}Nd$ ratios than oceanic arc magmas (Leeman, 1983; Plank and Langmuir, 1988; Hildreth and Moorbath, 1988; Turner and Langmuir, 2015a; Farner and Lee, 2017). Many of these compositional characteristics correlate strongly with crustal thickness (Turner et al., 2015a), and have been used as proxies to estimate changes in crustal thickness and rates of surface uplift though time (Profeta et al., 2015; Chiaradia, 2015; Chapman et al., 2015; Scott et al., 2018). Some of the compositional offsets between thick and thin-crusted arcs can be accounted for by higher extents of crystal fractionation and crustal assimilation in continental settings (e.g., Farner and Lee, 2017). However, other compositional differences persist in high Mg# arc lavas (Fig. 1a) that have not been extensively overprinted in the crust (e.g., Plank and Langmuir, 1988; Turner and Langmuir, 2015a; Turner et al., 2017; Schmidt and Jagoutz, 2017), suggestive of a mantle origin. Compositional differences among parental magmas from continental vs. oceanic arc settings have been attributed to variations in slab temperature (Ruscitto et al., 2012; Turner and Langmuir, 2015b; Schmidt and Jagoutz, 2017), different extents of mantle melting (e.g., Plank and Langmuir, 1988; Tormey et al., 1991; Turner et al.,

2016), subduction erosion (e.g., Stern, 1989), and heterogeneity of the "ambient" mantle (prior to the addition of subducted materials; e.g., Hickey et al., 1986; Ewart and Hawkesworth, 1987; Rogers and Hawkesworth, 1989; Hochstaedter et al., 2001; Pearce et al., 2007; Turner et al., 2017). Furthering our understanding of the thermal structure of subducting plates, the generation of wide-scale mantle heterogeneities, and the growth of the continental crust requires robust constraints on the relative influence of each factor in producing the enriched compositions of continental arc magmas.

The Andean Southern Volcanic Zone (SVZ) is an excellent natural laboratory in which to investigate how the thick crusts and lithospheres of active compressional plate margins affect the compositions of magmas added to the continents. The SVZ (33-46° S) is one of four volcanically active segments within the Andean Cordillera, where the Nazca Plate subducts under South America. It is commonly subdivided into three sub-segments: the northern, transitional, and southern SVZ (NSVZ, TSVZ and SSVZ respectively; Dungan et al., 2001; Fig. 2a). Between the latitudes of 42° S to 33° S (the focus of this study), crustal thickness increases from ~30 to 50 km (Fig. 2c), sub-arc slab depth increases from ~70 to 120 km (Tassara and Echaurren, 2012), and the lower plate age increases from 16 to 37 Ma (Völker et al., 2011), while trench sediment thickness decreases (Völker et al., 2013). In the NSVZ, seismic and heat flow data indicate that lithosphere thickness increases rapidly behind the arc, while behind the SSVZ, the lithosphere is thinner (Tassara and Echaurren, 2012; Valdenegro et al., 2019). As a result, the mantle wedge in the NSVZ is colder and deeper (Turner et al., 2016). There are also well-established geochemical gradients from the SSVZ to the NSVZ (Tormey et al., 1991; Hildreth and Moorbath, 1988; Hickey-Vargas et al., 2016, Fig. 2d-e). The trace element signatures of mafic SSVZ volcanics overlap those of oceanic arcs (Fig. 1a). In contrast, the more mafic TSVZ lavas have substantially elevated trace element abundances. The limited amount of trace element data from mafic NSVZ lavas (Fig. 1a; Hickey et al., 1986) suggest that this segment is even more enriched than the TSVZ, with compositions similar to the bulk continental crust and mafic to intermediate volcanics from other thick-crusted arc segments such as the Northern Cascades (Fig. 1a). Thus, the chemical variability between the SSVZ and NSVZ is analogous to the chemical offsets between island arcs, continental arcs, and the bulk continental crust.

While many studies have investigated the origin of along-strike compositional variability of the SVZ arc-front volcanoes (Lopez-Escobar et al., 1977; Hickey et al., 1986; Hildreth and Moorbath, 1988; Tormey et al., 1991; Jacques et al., 2014; Hickey-Vargas et al., 2016), the role of enrichment and heterogeneity within the ambient asthenospheric mantle (prior to the addition of subducted material) has received relatively little attention (Hickey et al., 1986; Jacques et al., 2014). Though often overlooked, the extent to which the compositions of continental arc volcanics are inherited from the ambient mantle has important implications

for models of crustal growth. If the trace element enrichment of continental arcs is inherited partially from the mantle, and not exclusively from extensive crystal fractionation and crustal remelting, a substantially smaller amount of material must be returned to the mantle to account for the continental mass balance (e.g. Sisson and Keleman, 2018). The amount of crustal recycling, in turn, has direct relevance for our understanding of the generation of large-scale mantle heterogeneity.

Heterogeneity of the upper mantle is commonly inferred from the trace element and isotopic compositions of mid-oceanic ridge basalts (MORBs) and ocean island basalts (OIBs; Zindler and Hart, 1986; Willbold and Stracke, 2010). OIB isotopic variability can generally be accounted for by a handful of isotopically distinct end-member components, such as the "enriched mantle" end-members (EM1, EM2; e.g., Zindler and Hart, 1986). Isotopic end-members are often modelled as the products of recycled lithospheric mantle, sediment, and ancient oceanic/continental crust (Willbold and Stracke, 2010). Despite additional tectonic complexity, there is also evidence for heterogeneity in the ambient mantle that feeds volcanic arcs. For example, a global compilation of samples from rear-arc provinces, filtered to minimize slab contributions (Turner and Langmuir, 2015b), form a linear array between Depleted MORB Mantle (DMM) and EM-1 type OIB compositions (Fig. 3a). As corner flow transports the mantle feeding rear-arc volcanism over hundreds of kilometres towards the arc-front (MacDougall et al., 2017), isotopic enrichment within rear-arc provinces indicates that ambient sub-arc mantle compositions also vary substantially (e.g., Woodhead et al., 2012). The Andean Southern Volcanic Zone (SVZ) rear arc exemplifies this enriched ambient mantle signature (Kay et al., 2013; Jacques et al. 2013, 2014; Søager et al., 2015a; Turner et al. 2017), with more enriched $^{87}Sr/^{86}Sr$ and $^{143}Nd/^{144}Nd$ ratios than any other rear-arc province globally (Fig. 3a).

This study investigates the petrogenesis of mafic lava samples from the volcanoes Don Casimiro and Maipo (within the Diamante-Maipo Caldera complex; 34˚S, Fig. 2b) in order to determine the geochemical character of high Mg# NSVZ magmas. These lavas from Don Casimiro and the basal portion of Maipo, which erupted immediately after the catastrophic formation (~150 ka) of the Diamante Caldera (Orozco et al., 2015), are among the most primitive ever sampled within the NSVZ (Fig. 4a; Hickey et al., 1986). Their primitive nature may indicate that the storage and eruption of these melts preceded the re-organization and maturation of crustal magma reservoirs beneath the Diamante caldera (analogous to post-collapse lavas at Campi Flegrei; Forni et al., 2018), or that ascending magmas utilized tension cracks formed during the collapse event (Jacques et al., 2014). Regardless of the exact mechanism permitting the eruption of mafic lavas within the thick-crusted NSVZ, these new samples provide an opportunity to characterise and explore the origins of the prominent chemical differences between the SSVZ and the NSVZ. As the chemical variability between the SSVZ and NSVZ is analogous to the chemical offsets between island arcs and continental arcs, exploring these

regional trends provides constraints on origins of magmatic enrichment within thickened continental subduction zones globally.

This study also incorporates samples erupted within the last 1 Myr from seven Argentinean monogenetic cones from the Payenia Volcanic Province (34.33˚ to 35.38˚S; Folguera et al., 2009). The origin of this rear-arc volcanism, located up to 350 km behind the NSVZ arc front, remains a topic of active research. Volcanism initiated in the earliest Miocene, associated with a period of shallow slab subduction, and continued into the Holocene (Kay and Copeland, 2006; Pallares et al., 2016). In the southernmost part of Payenia, it is generally accepted that the slab steepened towards the present-day dip of 33° (Tassara and Echuarren, 2012) by 5 Ma (Kay et al., 2005). Folguera et al. (2009) suggest that volcanism propagated northwards following extensional relaxation of the San Rafael block, while Gudnason et al. (2012) attribute the northward propagation of volcanism within Payenia to a northward delay in slab rollback. Despite uncertainty in the chronology and mode of magmagenesis of the SVZ rear-arc, the wide spatial distribution of volcanic products, along with their relatively primitive chemistry, provide vital constraints on the composition of the ambient sub-arc mantle beneath the SVZ (Jacques et al., 2013; Turner et al., 2017).

2. Samples and methods

Six samples were collected from the basal sequence of Maipo Volcano, the active stratovolcano at the centre of the Diamante-Maipo caldera, and nine from Don Casimiro Volcano, a small eroded stratovolcano located ~10 km SW of Maipo with activity restricted to preglacial times (Charrier, 1979; Fig. 2b). $^{40}Ar/^{39}Ar$ dates indicate that early activity at these centres was contemporaneous (Orozco et al., 2015). All lavas contain olivine and clinopyroxene phenocrysts within a glassy groundmass. The more evolved samples also contain plagioclase, oxides, and orthopyroxene (details in Appendix A). Samples were collected from seven separate monogenetic scoria cones in the northern rear-arc (34.3 to 35.4 ˚S; Fig. 2a). Olivine, clinopyroxene, and oxide phenocrysts dominate in these scorias, with microcrysts of plagioclase and alkali feldspar, and minor apatite.

All 22 samples were powdered for whole-rock analysis with an agate ball mill at the University of Oxford. Major element analysis was conducted using a PANalytical Axios Advanced X-ray fluorescence spectrometer at the University of Leicester (Knott et al., 2016). Powders were digested in clean labs at the University of Oxford for ICP-MS analysis. Ba and Sr were measured at a 1,200,000x dilution using a Thermo Element 2 ICP-MS, while all other trace elements were measured at a 6000x dilution on a Perkin Elmer NexION 350D quadrupole ICPMS (both at the University of Oxford). Four certified reference materials (CRMs; BCR-2, BHVO-2, AGV-2, and W-2a) were digested alongside these samples. Data was reduced using calibration curves generated from these 4 CRMs. Repeat solution analysis of one sample (n=19) and repeated digestions

indicate an analytical uncertainty of <3% (<5% for Cs), and calculated values for the CRMs yield concentrations within ±5% of the preferred values (Appendix C).

$^{87}Sr/^{86}Sr$ and $^{143}Nd/^{144}Nd$ isotope ratios were analysed for eleven samples at the University of Leeds. Following Sr and Nd purification, samples were loaded onto outgassed W (Sr) and Re (Nd) filaments, and analysed on a Thermo Scientific Triton-series multicollector mass spectrometer. NIST SRM-987, La Jolla and BHVO-2 were analysed throughout the session to monitor accuracy (Appendix C). Our analyses of these CRMs match preferred literature and 9-year TIMS laboratory values up to the 5th or 6th decimal place for $^{87}Sr/^{86}Sr$, and the 4th decimal place for $^{143}Nd/^{144}Nd$ ratios (Appendix C).

Olivine grains were analysed for major elements on a Cameca SXFive FEG-electron microprobe at the University of Oxford. St Johns Olivine and Fayalite were analysed as secondary standards to assess accuracy and precision (preferred values were within ±5%, with a precision of ~1%) . LA-ICP-MS olivine analysis was conducted at the University of Cambridge on a 193ESI Laser Ablation system coupled to a Nexion ICP-MS. Multiple secondary standards were run to monitor instrument drift, and accuracy and precision (preferred values were within ±10% for most elements, with a precision of ~5-10%). Additional analytical details included the values for repeated analyses of standards are provided in Appendix A and C

3. Results

The new Don Casimiro-Maipo samples are calc-alkaline basaltic andesites to andesites with whole-rock Mg#s between 60-70 (assuming Fe^{3+}/Fe_T=0.3; Holm et al., 2016), indicating that these samples have undergone only minor crystal fractionation from primary magmas (Fig. 4a). These new samples are some of the most primitive ever reported from the NSVZ, and greatly increase the number of known trace element and isotopic compositions for primitive NSVZ lavas (Mg#>60). There is little variation in SiO_2 (55.3–57.9 wt.%) within the sample set. Previous studies of the Diamante-Maipo Caldera (Hickey et al., 1986; Futa and Stern, 1988, Sruoga et al., 2005; Holm et al., 2014) have primarily sampled volcanics with significant europium anomalies ($Eu^* = [Sm_N \times Gd_N]^{0.5}$; Fig. 4b), indicating fractionation of plagioclase or mixing between primitive and evolved magmas (e.g., Turner and Langmuir, 2015a). In contrast, our higher Mg# samples have Eu/Eu*>0.9 (Fig. 4b). Olivine phenocryst compositions range from $Fo_{83.6-75.7}$ at the arc-front, which lie below the olivine-whole rock equilibrium line, indicating that some olivine accumulation has occurred. The highest Mg# Maipo lavas (Mg#~70) have compositions indicating the addition of up to 7 wt% Fo_{81} olivine to more evolved melts (Mg# ~60), and should not be regarded as “primitive” bulk compositions (Fig. 4a-b; Supplementary Fig. SB2; Appendix B; Hickey-Vargas et al., 2016). We regard the five Don Casimiro samples with the highest MgO, Eu/Eu* and Mg#s (circled on Fig. 4; 4.85-5.63wt% MgO) to be representative of the

most primitive magma compositions erupted within the Diamante-Maipo caldera. Indeed, their high Mg#s indicate that they are not far removed from mantle melts.

Like most arc magmas, mafic Don Casimiro-Maipo lavas have high abundances of Cs, Rb, Ba, U, Th, Pb, and Sr, and depletions in Nb and Ta relative to other elements of similar incompatibility during mantle melting (Fig. 1b). Highly incompatible trace element abundances of these lavas are elevated relative to typical mafic to intermediate samples from oceanic arcs and the SSVZ (Cs to Ce; Fig. 1a). Compared to other primitive SVZ samples, Don Casimiro-Maipo lavas also exhibit lower Cs/Rb ratios, smaller Zr-Hf depletions (Hf/Sm~0.9; Supplementary Fig. SB3), and significantly more enriched isotope ratios (higher $^{87}Sr/^{86}Sr$ and lower $^{143}Nd/^{144}Nd$ ratios; Fig. 3b). The isotopic compositions of the most primitive Don Casimiro samples from this study have lower $^{87}Sr/^{86}Sr$ and higher $^{143}Nd/^{144}Nd$ ratios than our Maipo lavas, and literature samples from throughout the Diamante-Maipo caldera (Fig. 3b).

Rear-arc scoria samples are basalts-trachybasalts (Fig. 4a; Mg#s of 58–71; if Fe^{3+}/Fe_T=0.15; Søager et al., 2015b). Another indicator of the relatively primitive nature of these rocks is the presence of olivine phenocrysts with forsterite contents between 80.6-90.1. These forsterite contents lie close to the equilibrium field predicted from whole-rock Mg#s (Supplementary Fig. SB2). Trace element patterns in the rear-arc show prominent subduction signatures (e.g., Nb-Ta depletion, Pb enrichment, and Th/Nb ratios up to 0.72), and concentrations even higher than Don Casimiro-Maipo lavas (Fig. 1b). As noted by Holm et al. (2016), rear-arc samples have slight depletions in the high field strength elements Zr and Hf, though such depletions are comparable to those observed within the SVZ arc front (Hf/Sm=~0.6; Supplementary Fig. SB3). $^{87}Sr/^{86}Sr$ and $^{143}Nd/^{144}Nd$ ratios of the new rear-arc samples plot between Don Casimiro-Maipo and literature SVZ data, and are mostly offset from the filtered rear-arc literature data to higher $^{87}Sr/^{86}Sr$ at a given $^{143}Nd/^{144}Nd$ ratio (Fig. 3b).

The new whole rock trace element and isotopic data from Don Casimiro-Maipo and rear-arc samples collected in this study is presented in Table 1. Complete geochemical analyses (including olivine compositions) are presented as a spreadsheet in Appendix C.

4. Discussion

The northward increase in crustal thickness in the SVZ provides the ideal setting to understand the relationship between primitive magma compositions and crustal thickness. However, the scarcity of geochemical data for mafic lavas in the NSVZ has hindered assessments of the composition of parental magma compositions, and thus the origin of regional geochemical variations. The more primitive nature of Don Casimiro-Maipo samples investigated in this study, combined with previous analyses of more evolved

rocks at this centre (Fig. 4a), finally allows deconvolution of the effects of crustal contamination from the role of mantle enrichment processes. In turn, alongside comparisons to literature data from the SSVZ, this provides a new opportunity to re-evaluate the relative contributions from crustal processing, mantle melting, slab fluxes, subduction erosion, and ambient mantle heterogeneity.

4.1. Crustal processing at Don Casimiro-Maipo

Hildreth and Moorbath (1988) suggested that mantle-derived magmas in the SVZ are processed in a melting, assimilation, storage, and homogenization (MASH) zone in the lower crust. In their model, mantle melts throughout the SVZ have similar compositions, and the enriched "baseline" composition of NSVZ magmas results from increased MASH processing in the north, where the crust is thickest. A compilation of samples from the entire Don Casimiro-Maipo caldera (this study and literature; Appendix E) indicates a role for crustal assimilation or mixing during fractional crystallization (AFC) in the petrogenesis of more evolved lavas. For example, the $^{87}Sr/^{86}Sr$ and $^{143}Nd/^{144}Nd$ ratios of Diamante Caldera lavas correlate with MgO and Eu/Eu* (Supplementary Fig. SB1). These geochemical trajectories can be recreated with a simple model where the compositions of sampled crustal lithologies (Lucassen et al. 2001; Lucassen et al., 2004) are mixed in variable proportions with primitive Don Casimiro-Maipo lavas (Fig. 4c-d). More complex assimilation models such as those considering the partial melting behaviour of different minerals and lithologies were not utilized, due to the uncertainty regarding the thermal properties and mineralogical composition of such a diverse range of basement lithologies. However, assuming some proportion of felsic lithologies represent melts of pre-existing crust, mixing trajectories provide an empirical representation of both simple and more complex pathways of crustal assimilation.

The MASH model proposed that the isotopic and trace element enrichment in even the most primitive NSVZ volcanics were caused by crustal assimilation and fractionation of parental magmas that are similar to SSVZ primary magmas. To test the power of the MASH model to explain the compositions of our new primitive NSVZ samples, we represent the composition of primitive SSVZ volcanics by an average composition of mafic samples from Villarrica. Villarrica was chosen as an end-member because it is one of the more mafic stratovolcanoes in the SSVZ, it's composition has been characterized by a number of previous studies (e.g., Hickey et al. 1986; Hickey-Vargas et al. 1989; Tormey et al., 1991; Morgado et al., 2015; Turner et al., 2016), and it has a similar trace element and isotopic composition to the other volcanoes of the SSVZ (Fig. 1a, Fig. 3b; Turner et al., 2016). We mixed the crustal lithologies which recreate the geochemical trajectories *within* the Diamante-Maipo Caldera into the composition of mafic Villarrica lavas as an initial test of whether assimilation into a primitive SSVZ magma can recreate the primitive Don Casimiro-Maipo lava compositions. These mixing trends produce rapidly decreasing K/Rb ratios prior to producing adequate enrichment in

$^{87}Sr/^{86}Sr$ ratios, and none reach high enough Rb/Y ratios to replicate the primitive Don Casimiro-Maipo lava compositions (Fig. 4c-d). Thus, assimilation of these lithologies cannot bridge the compositional gap between the SSVZ and NSVZ.

To test whether *any* plausible Andean crustal assimilant can bridge the compositional gap between the NSVZ (Don Casimiro-Maipo) and SSVZ (Villarrica), the compositions of 348 basement outcrops and basement xenoliths from the SVZ and the surrounding area (22-46°S) were compiled (Lucassen et al. 2001; Lucassen et al., 2004 and others; Appendix E). As above, assimilation was modelled by mixing the average composition of mafic Villarrica samples with each basement lithology (for mixing proportions between 0–100%). Only 14% of potential assimilants produce mixed compositions within $^{87}Sr/^{86}Sr$± 0.0001 and $^{143}Nd/^{144}Nd$± 0.00005 of the primitive Don Casimiro-Maipo average (Fig. 5a). Of these isotopically plausible mixed compositions, only 35% have Eu anomalies within the range of the primitive Don Casimiro-Maipo samples (Eu/Eu*>0.9). None of this subset of mixed compositions have trace element signatures resembling Don Casimiro-Maipo (Fig. 5b).

Incorporating crystal fractionation alongside these simple assimilation models also cannot account for these compositional offsets, because the resulting compositions deviate from primitive Don Casimiro-Maipo samples not only in overall elemental abundances, but also in a variety of incompatible element ratios that are not fractionated by early-crystallizing phases (e.g., Dy/Yb ratios; Davidson et al., 2007). Additionally, while models of recharging, evacuating and fractionation (REFC) magma chambers (Lee et al., 2014) could elevate incompatible element concentrations, this would drive prominent Fe enrichment, which is at odds with the high Mg#s observed in Don-Casimiro-Maipo and rear-arc samples. Finally, REFC would most probably occur in the deep crust (based on thermal constraints and the absence of Eu/Eu* anomalies in our samples). This would drive magma compositions towards peraluminous compositions which is inconsistent with our major element data.

It remains possible that the required MASH assimilant has evaded sampling within the Southern Andes. To address this possibility, we assess the chemical characteristics that a hypothetical assimilant must possess to bridge the compositional gap between the NSVZ and SSVZ. Assuming a maximum of 20% assimilation, based on the relatively high Mg#s of the most primitive Don Casimiro-Maipo lavas (assimilation drives cooling and crystal fractionation; DePaolo, 1981), any suitable assimilant must have greater than ~450ppm Zr, ~1420ppm Sr, and ~0.63wt% P_2O_5. It is improbable that crustal lithologies will possess these characteristics, because these elements typically become depleted, rather than enriched, during late stage crystal fractionation or crustal melting (Turner and Langmuir, 2015a). To illustrate this point, a compilation of all continental

granites, diorites, syenites, and monzonites in the GEOROC database (N~3000 with trace element data) was searched for suitable assimilants (considering only trace element abundances). Only 15 samples (0.5% of the entire compilation) possessed sufficient concentrations of Zr, Sr, and P_2O_5. Mixing of these lithologies with mafic Villarrica lavas produces compositions with erratic trace element patterns, testament to the complex petrological histories of these unusually enriched basement lithologies. None recreate the observed trace element pattern of Don Casimiro-Maipo, particularly the negative Nb-Ta anomaly (Fig. 5c). Thus, although crustal assimilation is common among more evolved samples from the NSVZ, the compositional offset between mafic NSVZ and SSVZ lavas is unlikely to have been generated by assimilation in the lower crust. The failure of the MASH model is most apparent when the full trace element signatures of regional crustal assimilants are considered, along with fundamental considerations regarding the production of enriched basement lithologies worldwide.

The $^{87}Sr/^{86}Sr$ and $^{143}Nd/^{144}Nd$ ratios of rear-arc samples presents further challenges to the MASH model's ability to explain the isotopic offsets between NSVZ and SSVZ samples. Interpreting the trace element and isotopic compositions of rear-arc samples is complicated by the sporadic infiltration of slab inputs (consisting of melts of AOC and sediment) to the rear-arc mantle (Jacques et al., 2013). However, by filtering a compilation of all published data from SVZ rear-arc monogenetic cones to remove samples with large slab inputs (Th/Nb>0.4), it becomes apparent that rear-arc $^{87}Sr/^{86}Sr$ and $^{143}Nd/^{144}Nd$ ratios plot along a "mantle array" between DMM and EM1-type ocean island basalts (Fig. 3a; Søager et al., 2013; 2015a-b; Søager and Holm, 2013; Kay et al., 2013; Jacques et al., 2013; 2014; Holm et al., 2014; Turner et al. 2017). This trajectory is not consistent with assimilation of available basement (e.g., Fig. 5b), because samples with high Mg#s are available at all points along the array. Additionally, unlike the arc-front samples, many of the primitive rear-arc volcanics contain highly forsteritic olivines, nearly in equilibrium with the mantle (Supplementary Fig. SB2). It is difficult to reconcile the presence of these primitive olivines with models invoking large amounts of crustal assimilation (e.g., 70% assimilation; Søager et al., 2013), as heat loss during assimilation would drive olivine compositions to lower forsterite contents. Additionally, rear-arc isotopic variability shows similar spatial trends to that observed at the arc-front, despite substantial longitudinal offsets (Fig. 6a-b). Crustal contamination cannot explain this similarity, as accretion and eastward migration of the arc-front since the Palaeozoic has produced a longitudinally fragmented basement, with different basement domains striking parallel to the coast (Kay et al., 2005). Assimilation of lithologies within these different basement domains would be expected to produce uncorrelated rear-arc and arc-front isotope systematics. In contrast, mantle flow paths *are* predicted to travel directly from the rear-arc to arc front, providing a coherent mechanism which accounts for the synchronized latitudinal changes in arc-front and rear-arc magmas. Thus, the coincidence of along-strike rear-arc and arc-front geochemical trends is one of the strongest pieces of

evidence that the enriched compositions of NSVZ magmas are derived from the mantle rather than the crust. Additional consideration will be given to this observation in section 4.5.

4.2 Assessing the slab and mantle melting contributions to SVZ compositional variation

As with other arcs, variable slab components and mantle melting processes may affect the chemistry of SVZ volcanics. The NSVZ mantle wedge is likely to have a lower maximum extent of melting than the SSVZ, because the thickened over-riding plate in the NSVZ forces high wedge temperatures to greater pressures (Turner et al., 2016). This should lead to enrichment of incompatible elements in the NSVZ (e.g. Tormey et al., 1991; Jacques et al., 2014; Turner et al., 2016). In addition to variability in mantle melt extent (F), the trace element compositions of primary arc magmas are influenced by the addition of slab inputs. For example, Jacques et al. (2014) attribute compositional variability between 38-43˚ S to varying slab fluxes. To assess whether the compositional differences between the NSVZ and SSVZ can be accounted for by varying F and/or slab components, it is useful to consider the maximum solution space generated by varying these parameters in tandem.

For this exercise, trace element concentrations and isotopic ratios were calculated using an adapted version of the mantle melting model of Turner and Langmuir (2015a). The compositions of subducted sediment and altered oceanic crust (AOC) were taken from the average isotopic and trace element compositions of sediment core ODP1232 (Turner et al., 2017) and NMORB (Gale et al., 2013). As numerical models indicate that SVZ slab top temperatures are well above the wet pelite and AOC solidi (Syracuse et al., 2010; Hermann and Spandler, 2007; Carter et al. 2015; Jacques et al., 2013; 2014), and only hydrous melt (as opposed to aqueous fluid) eclogite partition coefficients produce successful models of trace element abundances (Turner et al., 2017), it was assumed that slab melts (rather than fluids) were added to the mantle wedge. Slab melt compositions were calculated using the aggregate fractional melting equation and partition coefficients consistent with experiments (Kessel et al., 2005; Hermann and Rubatto, 2009; Skora and Blundy, 2010). Slab melts were then mixed with a depleted upper mantle composition assigned the trace element abundances of Workman and Hart (2005), and the isotopic composition of the rear-arc sample 126171 (Baseline Andean Mantle - BAM; Figs 3a, 6; 7; Søager et al., 2013). This sample defines the low Sr and high Nd end-member of the rear-arc array (Fig. 3a) and has a trace element composition that appears free of slab material (e.g., Th/Nb<0.06, Ce/Pb>25). Finally, the compositions of mantle melts were estimated using the batch melting equation, with experimentally-derived hydrous peridotite partition coefficients and melt reaction coefficients (further model details can be found in Appendix A).

Firstly, we consider the solution space for $^{87}Sr/^{86}Sr$ vs. $^{143}Nd/^{144}Nd$ ratios, which is simplified by the fact that these trajectories are not noticeably fractionated by variations in slab temperature, and are independent of melt extent. The pink field on Fig. 7a shows the solution space produced by variations in slab temperature and the proportions of slab melts. The isotopic composition of Villarrica (and most SSVZ) volcanics is encompassed within this field. However, TSVZ and Don Casimiro samples plot significantly below this field. As variable slab contributions predominantly drive wedge compositions to higher $^{87}Sr/^{86}Sr$ ratios at near constant or increasing $^{143}Nd/^{144}Nd$ ratios, another process is clearly needed to recreate the low $^{143}Nd/^{144}Nd$ ratios in TSVZ and NSVZ volcanics.

A similar solution space for trace element ratios is shown in Fig. 7b. The pink area encompasses the space made available by varying the proportions of a slab melts (with slab melting at ~800 °C) and F within reasonable bounds. F=0.04 was chosen as the lowest plausible mantle melting extent because F values <0.04 tend to produce alkali-basalt or silica-undersaturated major element compositions (e.g., Baasner et al., 2016). Villarrica samples plot within this field, and a model fit can be found that reproduces the entire suite of Villarrica incompatible trace elements and radiogenic isotope ratios (Figs. 7-8). This model fit also lies within the cluster of data defined by other SSVZ centres (purple dots, Fig. 7). While this model does not represent a unique solution for Villarrica, it does demonstrate that a feasible quantitative solution exists that is consistent with available experimental constraints. As in Fig. 7a, the compositions of most TSVZ and Don Casimiro-Maipo lavas fall outside of this solution space. The addition of sediment and AOC melt to the depleted mantle source can generate high La/Sm ratios, but only at excessively high Sr/Nd ratios (Fig. 7b). While reducing F can increase La/Sm ratios, even at F=0.04 there is no plausible trace element match to the Don Casimiro-Maipo lavas within this parameter space.

Slab temperatures might also affect the trace element compositions of SVZ volcanics. There are systematic changes in the slab age and depth beneath the SVZ arc front, both of which may lead to variability in the temperature of the slab surface beneath the arc front (Syracuse et al., 2010). Certain aspects of the trace element differences between Don Casimiro-Maipo and Villarrica are indeed suggestive of slab temperature variations. Compared to Villarrica, Don Casimiro-Maipo has low Cs/Rb and high Hf/Sm ratios (Fig. 1b). These element ratios are not substantially fractionated from each other during melting, and may indicate higher slab temperatures in the NSVZ. For example, Cs is highly mobile in low temperature aqueous fluids, and may have been disproportionally lost during early slab dehydration in the NSVZ, where the sub-arc slab is deeper (Savov et al., 2007; Spandler et al., 2007). Additionally, a hotter slab temperature can destabilize zircon during slab melting, which may lead to the less pronounced Zr-Hf depletions at Don Casimiro-Maipo (e.g., Hirai et al., 2018). The cyan field on Fig. 7b shows the expansion of the solution space for slab temperatures

hotter than 900˚C (calculated using the maximum measured experimental mobility of light rare earth elements in slab melts; see Appendix A). While the solution space at very high slab temperatures may shift toward higher La/Sm ratios at a given Sr/Nd ratio, the mafic NSVZ volcanic rocks remain well outside of the realm of possible solutions. Overall, the trace element and isotopic differences between mafic SSVZ and NSVZ volcanics cannot be recreated by variable slab additions and melt extents, even in combination. This indicates that the sub-arc mantle within the SVZ must be variably enriched to account for the prominent latitudinal variations in geochemistry.

4.3 Is there geochemical evidence for subduction erosion?

SVZ rear-arc volcanics form a linear array between MORB-like compositions and EM1-type OIBs in $^{87}Sr/^{86}Sr$ vs. $^{143}Nd/^{144}Nd$ space (Kay et al., 2013; Søager et al., 2015a; Fig. 3a), and both rear-arc and arc-front samples are characterized by similar along-strike variability in these isotope ratios (Fig. 6). As the isotopic offset between the mafic NSVZ and SSVZ samples is inconsistent with crustal assimilation or variable slab additions, an alternative mechanism is required to introduce an EM1-like contaminant to the mantle source of the SVZ. The origins of EM1-type OIBs are debated, with suggestions including deep recycling of lower continental crust (LCC), pelagic sediment and oceanic crust, or metasomatized subcontinental lithospheric mantle (Willbold and Stracke, 2010). The first suggestion is particularly apt, as it has been argued that the NSVZ endured extensive subduction erosion (the removal of upper plate material via abrasion and plucking by the lower plate) throughout the Cenozoic (Stern, 1989; Stern, 2011). Although the composition of the Andean LCC is relatively uncertain, an extensive compilation of regional basement compositions (Appendix E) constrains the likely compositional range of this reservoir. While these samples were collected from surface outcrops, Miocene episodes of tectonic thickening and under-thrusting have resulted in similar lithologies residing at deeper levels in the crust (Hildreth and Moorbath, 1991). Hence, this compilation can be used to assess the subduction erosion hypothesis, regardless of whether the UCC, LCC or the entire crustal column (Holm et al., 2014; 2016) on the leading edge of the South American plate undergoes recycling.

We assess the ability of subduction erosion to reproduce along-arc geochemical trends by mixing the composition of basement lithologies (Appendix E) into the composition of the Villarrica mantle source (following the addition of slab inputs) that produces the best model fit in Fig. 7. Melts of the resulting mixes were calculated using the model described above at conditions indicated by thermal models for Don Casimiro-Maipo (F=0.056, P=33kbar; Turner et al., 2016). This model scenario differs from our evaluation of crustal assimilation because crustal materials are mixed into the mantle source, rather than melts of the mantle. While trajectories of Sr-Nd isotope ratios are similar in both scenarios, additional of crustal materials has a much larger impact on the concentrations of incompatible trace elements in the subduction erosion

scenario. 11% of the mixed compositions pass within $^{87}Sr/^{86}Sr$±0.0001 and $^{143}Nd/^{144}Nd$±0.00005 of the most primitive Don Casimiro-Maipo samples (Fig. 9a). Only 15% of these isotopically plausible mixed compositions have Eu anomalies within the range of the primitive Don Casimiro-Maipo samples (Eu/Eu*>0.9), none of which recreate the concentrations of Y, Gd, Sm, Sr, Ba and $^{87}Sr/^{86}Sr$ ratios (Fig. 9b-c). This analysis demonstrates that no mixed composition with adequate trace element data plots within the range of the Don Casimiro-Maipo for $^{87}Sr/^{86}Sr$, and $^{143}Nd/^{144}Nd$ ratios, and trace element abundances.

While some previous studies in the NSVZ (e.g., Holm et al., 2014; 2016) have concluded that eroded continental material is the most plausible candidate for the enriched mantle end-member in this region, our analysis does not support this conclusion. This discrepancy arises from the fact that the newly sampled primitive Don Casimiro-Maipo lavas have Eu/Eu* close to 1. This implies that the low Eu/Eu* ratios of previous studies are a secondary overprint from plagioclase fractionation, magma mixing, or crustal assimilation, rather than a mantle source characteristic.

As with crustal assimilation during magmatic ascent, it is possible that the appropriate eroded crustal lithology has avoided sampling due to the restricted basement exposure in the SVZ. However, regional considerations indicate that LCC recycling is unlikely to produce the observed EM1-like enrichment. Willbold and Stracke (2010) present a model in which EM1-like isotopic compositions are produced by mixing LCC starting materials into normal MORB mantle. However, the success of this model requires recycled LCC domains to have been extracted and isolated from the mantle for >4 Ga, while the Chilenia and Cuyania terranes comprising the lower crust of the NSVZ-TSVZ are only of Grenvillian age (~1Ga; Ramos, 2010). This relatively young age causes typical Southern Andean basement to have $^{187}Sr/^{86}Sr$ ratios that are too high (relative to $^{143}Nd/^{144}Nd$) to serve as an appropriate end-member (see mixed compositions in Fig. 9a).

Rear-arc geochemical variability is also inconsistent with the subduction erosion hypothesis, because isotopic enrichment persists at distances exceeding 600 km from the trench. It is unlikely that material eroded at the trench could spread hundreds of kilometres towards the rear arc, in the opposite direction of corner flow (MacDougall et al., 2017). While eroded material may instead be carried down with the subducting slab and released alongside other slab inputs, in this case the enriched signature would co-vary with other slab components. Instead, at 550 km from the trench, rear-arc monogenetic samples have Ce/Pb ratios that range from 5 (similar to the arc front) to >20 (similar to MORBs; Fig. 10b), but retain $^{143}Nd/^{144}Nd$ ratios that are consistently enriched relative to DMM (Fig. 3a). Additionally, within a given latitude bracket, rear-arc $^{143}Nd/^{144}Nd$ ratios have limited variability, and do not correlate significantly with Ce/Pb ratios or other indices of slab additions. Finally, isotopic enrichment in both the rear arc and arc front increases in a

reasonably symmetrical, coherent fashion on either side of a pronounced minima at 39° S (Fig. 6; Turner et al., 2017). Although it has been suggested that subduction erosion increases northwards (Stern, 1989), this phenomenon cannot account for the increase in enrichment south of Villarrica (Fig. 6). The spatial systematics of rear-arc compositions are therefore also inconsistent with subduction erosion.

Overall, when the full array of trace element abundances and isotopic ratios are considered, subduction erosion cannot recreate the notable geochemical trends in rear-arc and arc-front data. This may indicate that the extent of subduction erosion has been over-estimated for the SVZ. In some cases, erosion rates are calculated based on the assumption that the distance between the trench and the arc front remained constant throughout the Miocene (Stern, 1989). However, more recent geophysical models find that arc-front migration relative to trench location might be a common process (e.g., Karlstrom et al., 2014), and the locus of subduction-related volcanism has also likely been influenced by variability of the slab angle over this same interval (Kay et al., 2006). Alternatively, it is possible that subduction erosion did indeed influence the mantle wedge composition at some point in the Miocene, but corner flow towards the arc has since flushed the present-day mantle wedge of eroded material. Regardless of the explanation, the range of plausible geochemical signatures that would be produced by subduction erosion are inconsistent with the along-strike enrichment trend of the SVZ, and thus some other mechanism is required to explain SVZ geochemical variability.

4.4 EM1-type enrichment from a sub-continental lithospheric mantle source

An alternative source for the enriched EM1-like mantle signature of the NSVZ is the recycling of metasomatised subcontinental lithospheric mantle (M-SCLM). The infiltration of low-degree mantle melts (F~0.005) into the base of the lithospheric mantle produces enriched incompatible element concentrations, which rapidly evolve to EM1-like isotopic compositions (McKenzie and O'Nions, 1995; Turner et al., 2017; blue and green lines on Fig. 11). Unlike crustally-derived materials, M-SCLM provides a more homogenous end-member composition that is capable of recreating the remarkably coherent geochemical trends observed in the SVZ (Rogers and Hawkesworth, 1989; Turner et al, 2017). M-SCLM material may be stored for long periods in the lithospheric mantle before it is returned to the asthenosphere by delamination, or erosion driven by corner flow.

Field evidence supports the hypothesis that the SCLM surrounding the SVZ has EM1-like isotopic affinities. Three geographically separated suites of isotopically enriched igneous rocks across South America have been interpreted as direct melts of the enriched SCLM (see Fig. 2a):

1) Alkaline igneous rocks erupted near the edges of the Rio Apa-Luis Alves (Brazil and Paraguay) and Sao Francisco Cratons (Brazil; Gibson et al., 1995; 2005; Carlson et al., 1996).
2) Mesozoic metabasites from the Southern Rift (Argentina; Lucassen et al., 2002).
3) Carboniferous granitoids from the Santo Domingo Complex of the Coastal Batholith (Chile; Parada et al., 1999).

The $^{87}Sr/^{86}Sr$ and $^{143}Nd/^{144}Nd$ ratios of samples from these regions plot as a linear extension of the SVZ rear-arc array (Fig. 11), and cannot be accounted for by addition of variable slab components or assimilation of available basement. The remarkable alignment of these lithologies in isotopic space, despite being geographically separated by hundreds to thousands of kilometres, suggests that M-SCLM east and north of the SVZ has relatively homogeneous EM1 affinities. The isotopic trajectory of these SCLM melts is consistent with the expected isotopic evolution of SCLM enriched by low-degree mantle melts (Turner et al., 2017; Fig. 11). In contrast, the field produced by addition of sampled basement lithologies to the mantle has higher $^{87}Sr/^{86}Sr$ at a given $^{143}Nd/^{144}Nd$ ratio than the array of SCLM-melts and rear-arc volcanics, and a significantly broader trajectory (grey field, Fig. 11).

Rather than attempt to estimate the full trace element composition of very low-degree metasomatising mantle melts, a proxy for the composition of mantle domains which has been enriched by M-SCLM melts was estimated by inverting for the mantle source composition of Gough Island EM1-type OIB volcanics (Turner et al., 2017). The archetypal EM1-type enrichment at Gough has been specifically linked to the incorporation of subcontinental lithospheric mantle with compositions similar to that sampled by magmas in South America (Gibson et al., 2005; Boyet et al., 2019). Trace element and isotopic ratios of the inverted Gough source composition were subsequently adjusted within the limits of EM1-like ocean island basalts (Stracke et al. 2003; Willbold and Stracke, 2010) to produce a generic EM1 source (see Appendix A). Including EM1-like mantle heterogeneity as an additional parameter expands the solution spaces on Fig. 7a-b (grey fields) to overlap the composition of primitive Don Casimiro-Maipo lavas. Furthermore, a model fit incorporating this EM1-type mantle component recreates the isotopic composition and entire suite of incompatible trace element concentrations at Don Casimiro-Maipo (Figs. 7–8). As with the model fit for Villarrica, this does not represent a unique solution, but does suggest that the observed geochemical enrichment at Don Casimiro-Maipo is quantitatively consistent with all available constraints, unlike models relying upon MASH, LCC recycling, or variable slab components.

The addition of M-SCLM to the mantle by erosion or delamination at the base of continental cratons behind the volcanic arc also accounts for spatial trends in rear-arc and arc-front geochemistry. Turner et al. (2017) proposed two explanations for the gradual decline in isotopic enrichment towards a distinct minimum at 39°

S (Fig. 6). Firstly, they note the presence of a Permian terrane suture at 39° S (Rapalini et al., 2010). It is possible that M-SCLM was lost during rifting or subsequent collision between cratonic blocks (Fig. 12a). Secondly, a vertical and horizontal slab tear at ~39° S has been inferred from seismic imaging (Pesicek et al., 2012). If M-SCLM material was entrained into the mantle flowing towards the SVZ in reasonably similar quantities along strike (in contrast to the suture model), upwelling of depleted Pacific mantle which has not interacted with M-SCLM through these features could dilute the EM1 signature. The upwelling, depleted mantle would then spread northwards and southwards, perhaps aided by toroidal flow (Zandt and Humphreys, 2008), resulting in a gradual northward and southward increase in enrichment (Fig. 12b). This upwelling material could also produce the magnetotellurically imaged "plume" in the rear-arc (Burd et al., 2014). Geochemical signatures associated with upwelling through a slab window in the Kula Volcanic Field (W. Anatolia, Turkey) are traced over >250 km (Klaver et al., 2016), similar to the distances observed here.

4.5 A unified model for the SVZ arc-front and rear-arc

The preceding sections have shown that the first-order geochemical variability in the SVZ arc-front and rear-arc is consistent with the mixing of EM1-type and isotopically depleted mantle end-members. This is similar to the proposal of Jacques et al. (2013, 2014), though by including the influence of ambient mantle enrichment on trace element abundances, our model does not require substantial variations in the composition of slab components, or exceedingly low extents of melting to account for NSVZ arc-front compositions. In contrast to the unified models of arc-front and rear-arc geochemistry presented in Jacques et al. (2013, 2014) and this study, other models have proposed unique processes specific to particular regions of the rear-arc. For example, Søager et al. (2015a;b) invoke the presence of a distinct “Rio Colorado” mantle component in Southern Payenia, Søager et al. (2013;2015a) suggest that rear-arc basalts of the Nevado volcanic field (~35-36˚S) have assimilated up to 70% LCC, and Holm et al. (2016) conclude that both enriched mantle and eroded crust produce geochemical variation observed in the Northern Segment of the rear-arc (~34-35 ˚S). To assess whether these region-specific observations can be accounted for by our unified model, it is important to consider the characteristics of across-arc geochemical trends and temporal variability in SVZ subduction geometry.

The extent to which slab materials have infiltrated the rear-arc mantle can be investigated using trace element ratios sensitive to the addition of slab melts (e.g., Th/Nb, Th/La, and Ce/Pb ratios; Johnson and Plank, 1999; Plank, 2005; Fig. 10a). Remarkably, while these slab-sensitive ratios generally show declining slab fluxes with increasing trench distance, some cones retain elevated Th/La and Th/Nb ratios and low Ce/Pb ratios at nearly 600km from the trench (Fig. 10b). Strong slab signals in older (>5 Ma) Andean rear-arc

volcanics have been interpreted to result from transient variations in the dip angle of the subducting slab (Kay et al., 2006). However, the rear-arc samples of this study were likely erupted between 0.01–0.7 Ma (Folguera et al., 2009), yet still exhibit trace element patterns that clearly indicate the addition of slab melts (Figure 1b). One possible explanation for this phenomenon is that this slab signal is still a remnant from the Miocene period of shallow subduction, and not related to the present-day slab geometry (Søager et al., 2013; Holm et al., 2016). However, It is difficult to reconcile this model with expectations from geodynamic models and the chronology of arc-front volcanism

In Southern Payenia, it is generally accepted that the slab steepened towards its current configuration at ~5 Ma (Kay et al., 2005). However, Gudnason et al. (2012) attribute the northward propagation of quaternary rear-arc volcanism to a significant delay in slab rollback in this region, while Folguera et al. (2009) suggest that the recent volcanism behind the NSVZ is due to extension collapse. Of these proposals, only the model of Folguera et al. accounts for activity within the Diamante-Maipo caldera, which has been essentially uninterrupted since the Late Miocene (Sruoga et al., 2005). This near continuous activity indicates that the NSVZ slab geometry is unlikely to have shifted substantially from its current position over the past 5 Ma. Over 5 Myrs, given a convergence rate of ~70 km/Ma, the mantle wedge should have turned over ~350 km between the establishment of the current slab configuration, and the eruption of the youngest rear-arc volcanics. As older slab-derived materials would have been effectively flushed from the wedge before the generation of the melts sampled in this study, slab signatures in recent rear-arc volcanics were most likely derived from the slab in its current geometry.

Variation in slab temperature fractionate many elements in slab melts (e.g. Hermann and Rubatto, 2009), so provide an additional set of constraints on the dynamics of the SVZ mantle wedge. If across-arc slab temperature variations are in accord with SVZ thermal models (Syracuse et al., 2010), then Th/La ratios in slab melts may increase by ~25% from the arc-front to the rear-arc, and Th/Nb ratios by nearly an order of magnitude (Hermann and Rubatto, 2009). This variability in the composition of slab melts should result in rear-arc and arc-front lavas following distinct mixing trajectories. Yet, rear-arc samples lie on mixing lines between the modelled arc-front slab melt composition (as used in the model in Fig. 8) and an ambient mantle with varying amounts of EM1-like enrichment (Fig. 10a). The high slab temperatures beneath rear-arc cones should also destabilize zircon (e.g., Hirai et al., 2018). However, rear-arc samples have Zr-Hf anomalies similar to TSVZ and SSVZ arc-front volcanoes (Supplementary Fig. SB3). These observations imply that the slab components reaching the rear-arc and arc-front mantle sources were extracted from the slab at similar temperatures.

Thus, the slab component observed in northern rear-arc cones was likely derived from the slab in its current geometry, but was unlikely to have been extracted from the slab directly beneath the cones. Two-phase thermo-mechanical models provide an explanation for this phenomenon. The mantle source at the arc front may be influenced by slab materials that were extracted from the slab beyond the arc front, and then deflected towards the trench along compaction pressure gradients (Wilson et al., 2014). The rear-arc asthenosphere is plausibly influenced by slab melts extracted at shallower depths and then transported away from the trench in zones of low porosity (Cerpa et al., 2017; Fig. 13b). It is also possible that slab materials could be transported non-vertically by "mélange diapirs". However, Cruz-Uribe et al. (2018) found that melts of such diapirs have >50 wt. % SiO_2, >18 wt. % Al_2O_3, and <8 wt. % MgO, while the most primitive SVZ rear-arc basalts have >10 wt. % MgO, <48 wt. % SiO_2, and <15 wt. % Al_2O_3, as is typical of arc alkali basalts generated by low degrees of melting from a lherzolite source (e.g., Baasner et al., 2016). The experimental melts also have positive Zr-Hf anomalies, unlike the negative Zr-Hf anomalies of SVZ rear-arc lavas (Fig. 1b). Overall, the geochemical systematics of SVZ rear-arc volcanics appear to be most consistent with a strong role for slab melting followed by advective transport, compaction channelling, and generally non-vertical transport of slab-derived materials through the wedge, which provides support for recent numerical models of two-phase flow (Cagnioncle et al., 2007; Wilson et al., 2014; Cerpa et al., 2017).

Given the general viability of our unified SVZ model, where geochemical trends in rear-arc and arc-front lavas can be accounted for by variations in the composition of the ambient mantle, slab additions and melting variations, it is worthwhile to consider whether this model can also account for the observations that have motivated region-specific models. Here, we limit this discussion to trends (Fig. 14a-c) that have been interpreted to form by extensive lower crustal assimilation (up to 70%; Søager et al., 2013; Søager et al., 2015a). While rear-arc compositions on these plots appear to trend toward the compositions of certain lower crustal xenoliths (Kay et al., 1996), calculated mixing lines with these xenoliths are strongly hyperbolic, and deviate substantially from rear-arc compositions (Supplementary Fig. SB5). While "adjusted" lower crust compositions have been proposed to mediate such discrepancies (Søager et al., 2013), these adjusted compositions resemble neither generic models of the LCC (e.g., Rudnick and Gao, 2003), nor the actual compositions of Andean basement samples (Supplementary Fig. SB6). These observations, along with the general difficulty of maintaining high Mg# bulk compositions and highly forsteritic olivines while enduring such large amounts of crustal assimilation, motivate a re-examination of the assimilation model.

Our analysis suggests that the regional systematics identified by Søager et al. (2013; 2015a; 2015b) can be fully accounted for by the variations expected from slab fluxes, mantle melting extents, and the ambient mantle. On Figure 14a, both axes are controlled by mantle and slab components, while the y-axis (La/Sm) is

also affected by variations in F. The arc-front volcanics have relatively uniform slab contributions, so follow a trajectory determined by F and the ambient mantle. Many of the rear-arc samples overlap the arc-front data. However, when slab additions are diminished, the extent of mantle melting often drops to very low values (Jacques et al., 2013), which drives up La/Sm ratios. This is apparent from the similarly high La/Sm ratios of basalts from the Gough Island chain. Like Andean rear-arc lavas, Gough lavas are alkali basalts produced by low-F melting of garnet lherzolite (Søager et al. 2015a; Boyet et al., 2019). In Gough, the very low degree melting occurs within a region of enriched ambient mantle, leading to lower $^{143}Nd/^{144}Nd$ and even higher La/Sm ratios than the SVZ rear-arc volcanics. Similar systematics can account for variability on Figure 14b, though the divergence between arc-front and rear-arc compositions is less apparent here, as both low-F melt generation and bulk slab additions skew compositions toward very high Th/Sm ratios (much higher than seen in the Gough basalts). Thus, the variability on both Figs. 14a and b are easily accommodated without a crustal assimilant.

Unlike Th/Sm and La/Sm ratios, the highly-incompatible element ratios on Figure 14c are less affected by variations in melt extent, and can be accounted for by variations in slab flux and mantle enrichment alone. Ba/Th is particularly sensitive to small variations in the compositions of subducting slab materials and temperatures of slab melting (e.g., Carter et al., 2015; Patino et al., 2000). This is evident from the high Ba/Th mafic enclaves erupted at Longaví Volcano (36.2˚ S; SSVZ), which are thought to be representative of parental magmas at this centre (Rodríguez et al., 2007). Rodríguez et al. (2007) demonstrate that these enclaves reflect input of a particularly high Ba/Th slab component to the mantle, and suggest this is caused by the proximal subduction of the Mocho Fracture Zone (Fig. 14d). Hydrothermal alteration, which was likely enhanced along the fracture zone, produces elevated Ba abundances in both ocean crust and sediment (Kelley et al., 2003; Plank et al., 2013). Alternatively, the fracture zone may introduce an additional high-Ba fluid component to the wedge. Subducting fracture zones have inevitably swept along the arc over time, causing transient geochemical signals among sensitive slab tracers in local volcanics (Fig. 14d). Given the large range in the Ba/Th ratio of the slab component, there is no need to invoke extremely large quantities of lower crustal assimilation (>70%) to account for regional systematics. While geochemical variability, when considered on a small enough scale, necessarily requires case-specific ad-hoc explanations, the regional trends of the SVZ appear consistent with the relatively simple three parameter model developed here (Fig. 7; Fig. 10; Fig. 14) which incorporates processes seen in subduction zones worldwide.

5. Conclusions

The origins of trace element and isotopic enrichment in thick-crusted continental arcs have profound implications for the formation of the continental crust and the petrogenesis of evolved magmas. The new

high-Mg# samples characterized here provide valuable constraints on the compositions of parental magmas from the thick-crusted Northern SVZ (NSVZ). While evolved NSVZ samples underwent crustal assimilation during fractional crystallization, the geochemical offsets between the most primitive Southern SVZ (SSVZ) and NSVZ volcanics cannot be produced assimilation of any basement lithologies either within the Southern Andes, or globally. Similarly, while variations in the extent of mantle melting and subtle differences in slab additions may arise due to the thicker lithosphere and deeper slab in the NSVZ, the solution space made available by these parameters does not encompass the trace element or isotopic compositions of mafic Don-Casimiro Maipo samples. Only models incorporating an enriched ambient mantle domain that is compositionally similar to the mantle source of EM1-type OIBs can recreate the observed isotopic and trace element enrichment in mafic samples from Don Casimiro-Maipo. Coincident arc-front and rear-arc regional variations in isotopic enrichment suggest that this signal arises from the ambient mantle. A forward model based on an inversion for an EM1-like mantle source successfully reproduces the isotopic composition and trace element composition of Don-Casimiro Maipo, demonstrating that this interpretation is consistent with available experimental constraints.

The isotopic trajectory of rear-arc lavas is co-linear with other South American lavas thought to represent melts of metasomatized sub-continental lithospheric mantle (M-SCLM). This supports a model in which the enriched mantle source is derived from the addition of M-SCLM material to a depleted mantle wedge by erosion or delamination from the cratonic lithosphere behind the arc. An alternative scenario in which the EM1 signal results from subduction erosion of continental material produces unsuitable isotopic systematics and erratic trace element patterns. Additionally, subduction erosion of fragmented basement domains fails to account for coherent along and across-arc geochemical variations. However, unlike the longitudinally fragmented and highly heterogeneous Andean basement, the composition of the M-SCLM appears to be relatively homogenous across a large area of South America. Thus, unlike subduction erosion or crustal assimilation, the trench-ward flow of variably enriched mantle domains by corner flow accounts for the coherent latitudinal variations in the isotopic ratios of arc-front and rear-arc lavas.

In addition to chemical diversity induced by variable M-SCLM addition, rear-arc cones receive highly variable slab inputs that are surprisingly similar in composition to the arc front (Fig. 10). This, along with variable melt extents, accounts for the offset trajectories of rear-arc and arc-front lavas, and provides support for recent two-phase flow models indicating non-vertical transport of slab materials (Cagnioncle et al., 2007; Wilson et al., 2014; Cerpa et al., 2017). This unified model of rear-arc and arc-front geochemical variability is able to account for the geochemical variations previously attributed to a variety of region-specific processes.

Overall, we demonstrate that the enriched trace element and isotopic compositions of primitive lavas in the thick-crusted NSVZ are produced by low-degree melting of an enriched ambient mantle that is metasomatized by slab melts (Turner et al., 2017), rather than crystal fractionation and crustal assimilation. The similarities between the trace element signatures of primitive NSVZ lavas and the bulk continental crust (Fig. 1) implies that ambient mantle enrichments may play a major role in the origin of enriched continental compositions globally. Revaluation of enriched signatures in primitive lavas of other thick-crusted arcs (e.g., Cascades, Mexico, Guatemala, Colombia) will allow assessment of the global importance of ambient mantle enrichment. If similarities with the SVZ are found, models of continental crust generation and elemental cycling within the silicate earth will require re-evaluation.

Acknowledgments

The authors acknowledge NERC grant 'Mantle volatiles: processes, reservoirs and fluxes' (NE/M000427/1) for funding, and PW acknowledges her NERC DTP studentship (NE/L002507/1) to Cambridge University for support during the writing of this manuscript. The authors thank Melissa Murphy for help with clean lab chemistry, Sally Gibson for use of the LA-ICP-MS, Jason Day for helping with analysis, and Patrick Sugden for assistance with sample preparation for Sr and Nd isotopic analysis in Leeds. We also thank Lucy McGee, Nina Soager, Gary Michelfelder, and Oliver Nebel, as well as several anonymous reviewers for very helpful comments which significantly improved the quality of this manuscript, and Rosemary Hickey-Vargas for editorial handling.

Research Data

The whole-rock major element, trace element and isotopic data, and olivine EPMA and LAICPMS data collected in this study are provided as an excel spreadsheet in Appendix C (alongside information on analyses of standards). Literature databases used in this study are provided as excel spreadsheets in Appendix D and E.

Figure Captions

Fig. 1– Incompatible trace element "spider diagrams", normalized to D-MORB (Gale et al., 2013). a) Literature data for Don Casimiro-Maipo (Hickey et al., 1986) has incompatible trace element abundances comparable to bulk continental crust (Rudnick and Gao, 2003) and the Northern Cascades (samples with Mg#>0.64 for Fe^{3+}/Fe_T=0.8, and Eu/Eu*>0.9 are shown for Mt Ranier and Mt Hood; Sisson et al., 2014; Baggerman and DeBari, 2011). Don Casimiro-Maipo shows significantly more enriched trace element abundances than the TSVZ, SSVZ, and the majority of island arcs (GEOROC compilation). Villarrica, which has a similar trace element signature to other SSVZ centres (Llaima, Puyehue and Osorno shown here; Turner et

al. 2016), is used as a representative SSVZ end-member in figures 3, 4, 5, 7, 8 and 9. b) Trace element data collected in this study for 7 rear-arc cones, and the five most primitive samples from Don Casimiro-Maipo (circled on Fig. 4). The observed HREE depletion in Don Casimiro-Maipo samples indicates that garnet is residual in the mantle source during mantle melting. Rear-arc samples show distinctive arc-like signatures, and even greater trace element enrichment than Don Casimiro-Maipo samples.

Fig. 2-Geographical context and sample locations. a) Map of the SVZ, showing the segment boundaries defined by Dungan et al. (2001). The locations of arc-front and rear-arc samples investigated in this study are shown, along with the locations of arc-front volcanoes passing the filters of Turner et al. (2016). The geographical regions containing inferred M-SCLM melts (see Fig. 11) are overlain in purple, yellow and cyan. Base map from GEOMAP APP. b) Sample locations of Don Casimiro and Basal Maipo lavas within the Diamante-Maipo Caldera Complex. Imagery from Google Earth. c) Moho depth (from the model of Tassara and Echaurren, 2012) vs. volcano latitudes projected along the vector of convergence to the trench. d-e) Incompatible major and trace element concentrations for the most primitive lavas (Turner et al. 2016, and this study) increase northwards, mirroring changes in crustal thickness.

Fig. 3- a) SVZ rear-arc samples which are not dominated by slab inputs (Th/Nb<0.4) plot along the “mantle array”, between DMM and EM1-type ocean island basalts. These rear-arc samples greatly extend the isotopic range observed among average rear-arc compositions from other arcs (black dots; Turner et al., 2017). Literature values from Don Casimiro-Maipo lie at the enriched end of the global rear-arc array (Hickey et al., 1986). The blue and pink fields envelop EM1 and EM2-type ocean island basalts from Stracke et al. (2003). The enriched isotopic end-member used for quantitative modelling is from Pitcairn (57DS9; Stracke et al., 2003). The isotopic composition of the Baseline Andean Mantle (BAM) end member was taken from a SVZ rear-arc sample with no trace of a slab contribution (e.g. Th/Nb<0.06, Ce/Pb>25; Søager et al., 2013; sample 126171). The Nazca Plate sediment composition is the average of ODP1232 (Turner et al., 2017). b) Don Casimiro and Maipo and rear-arc isotopic data from this study. Literature data from Villarrica and the rest of the SVZ that pass filters indicating they are not substantially affected by crustal contamination or mixing (Turner et al., 2016) are overlain. The filtered rear-arc samples shown in a) are also shown in b), along with unfiltered data from the entire Diamante-Maipo Caldera.

Fig. 4- a) Don Casimiro-Maipo samples from this study are high Mg# basaltic andesites. The two samples circled in red have major element characteristics indicative of olivine accumulation (Supplementary Fig. SB2). The five most primitive samples used to characterize the composition of primitive magmas from Don Casimiro-Maipo are circled in grey. Rear-arc samples are primitive basalts-trachybasalts. Mg#s were

calculated assuming Fe^{3+}/Fe_T =0.3 for the arc-front (Holm et al., 2016), and Fe^{3+}/Fe_T =0.15-0.3 for the rear-arc (Søager et al., 2015b, cyan and blue triangles respectively). b) Eu anomalies are negligible in the most primitive samples of this study (>0.9), whereas the majority of literature samples from the Diamante-Maipo caldera show substantial negative Eu anomalies. Eu/Eu* was calculated with $Eu^* = (Sm_N \times Gd_N)^{1/2}$ or with $Eu^{**} = (Sm_N^2 \times Tb_N)^{1/3}$ where no Gd data was reported. In both cases, element concentrations were normalized to CI chondrite (McDonough and Sun, 1995). c-d) Mixing arrays between eight SVZ basement samples and primitive Don Casimiro-Maipo samples encompass the chemical diversity within the Diamante-Maipo Caldera (basement compositions from Lucassen et al. 2001; # 84-31-1, 84-31-2, 84-42-1, 84-42-11, and Lucassen et al. 2004; # 00-77, 00-55, 00-58 and 00-05). However, mixing between the same 8 samples and primitive Villarrica lavas (grey lines) do not pass through primitive Don Casimiro-Maipo samples. Models originate from the primitive average of Don Casimiro-Maipo and Villarrica lavas. Error bars in c) show ± 1σ of the variation among primitive samples.

Fig. 5-Crustal assimilation models. a) Mixing lines between 348 crustal lithologies thought to be representative of SVZ basement (compiled from GEOROC and other sources) and the average composition of primitive Villarrica lavas. Only a small proportion pass near Don Casimiro-Maipo. b) Trace element patterns of the mixed compositions which have isotopic ratios close to Don Casimiro-Maipo (red lines in a), as well as Eu/Eu*>0.9. Mixtures providing a reasonable match to the La-Ce concentrations (cyan lines) have trace element patterns that are completely distinct from those of primitive Don Casimiro-Maipo lavas. c) Trace element signatures of mixed compositions for the small subset of the ~3000 plutonic rocks from GEOROC that have sufficient concentrations of Zr, Sr and P_2O_5 to recreate the enrichment of these elements at Don Casimiro-Maipo. Mixed compositions were calculated for the % mixing required to recreate Zr concentrations. All produce erratic trace element patterns that are dissimilar to those observed at Don Casimiro-Maipo.

Fig. 6 - Across and along-arc variations in rear-arc isotopes. a-b) Rear-arc isotopic ratios form latitudinally coherent trends, with statistically significant trend lines ($p<0.005$). A pronounced minimum in $^{87}Sr/^{86}Sr$, and a maximum in $^{143}Nd/^{144}Nd$ is observed at ~39° S, with reasonably linear and symmetric changes to the north and south that can be explained by variable EM1 enrichment (pink arrows). Scatter about these first order trends results from variable slab fluxes (and possible local heterogeneity) within the rear-arc. The blue bar shows the range of bulk slab compositions for a mix of 20% sediment melt, 80% AOC melt, incorporating the ± 1σ variation of the sediment composition from ODP1232 (Turner et al., 2017). Rear-arc samples from this study fit within the regional trends. Arc-front centres lie close to the rear-arc best fit line, showing that these spatial trends in enrichment are also present at the arc-front. The deviation in $^{143}Nd/^{144}Nd$ between the rear-

arc and the arc-front south of 39° S likely results from the sparse sampling of rear-arc centres, making it difficult to resolve regional trends from local variations in heterogeneity. This offset may also reflect the smaller slab inputs to the southern rear-arc compared to the southern arc-front.

Fig. 7 – Trace element and isotopic solution spaces produced by varying the composition of slab melts, melt extents, and the composition of the ambient mantle. a) The pink field represents the maximum isotopic solution space available by the addition of varying additions of slab melt (up to 2% sediment melt, 10% AOC melt) to a depleted mantle ("baseline ambient mantle"; BAM), with a trace element composition of DMM, and isotopic composition of Sample 126171 (Søager et al., 2013). Variable slab temperatures have very little effect on the size of this isotopic solution space, so are not shown. The grey field represents the additional solution space made available by the addition of an EM1-type mantle domain to the composition of BAM. b) The pink field represents the maximum trace element solution space available by varying slab additions as in a), in addition to variations in F between 0.04 and 0.3. The teal field represents the additional solution space made available by an increase in slab temperature (with a change in the partition coefficients of La, Sm, and Nd; see Appendix A). As in a), the grey field represents variable enrichment by an EM1-type mantle source. In both figures, it is clear that only the addition of an EM1-type mantle source to the sub-arc mantle can recreate the composition at Don Casimiro-Maipo. The diamonds represent the best model fits for Villarrica (F=0.1, 7.5% slab addition consisting of 17% sediment, with no EM1 enrichment) and Don Casimiro-Maipo (F=0.056, 7.5% slab addition consisting of 23% sediment, with 80% EM1 enrichment). The full trace element signatures of these models are shown in Fig. 8.

Fig. 8 – Trace element modelling results. The trace element composition of Villarrica can be well matched at F=0.1 with addition of 7.5% slab melt consisting of 17% sediment (black lines). The extreme trace element enrichment at Don Casimiro-Maipo is best recreated by addition of 80% enriched source, and slight changes in the composition of slab additions (23% sediment vs. 17% at Villarrica; grey lines). The mantle melting model includes a parameterization for changing garnet proportions based on melt depths (Gt=0.0067*GPa+0.0017); we assume that melt production at Don Casimiro-Maipo and Villarrica occur at 3.3 GPa and 2.2 GPa respectively (Turner et al., 2016). The solid black lines in both figures represents the best model fit for each centre at the enrichment and proportions of AOC:SED mentioned above using low temperature slab partition coefficients. This provides the best match for Villarrica. The dashed grey lines represent the model fit for each centre at increased slab temperatures, assuming 70% loss of Cs in the forearc. This provides the best model fit for Don Casimiro-Maipo. Model envelopes were produced by adding and subtracting 1σ of 33 measurements of ODP1232 (Turner et al., 2017). Melting conditions were generated directly from the physical modelling results of Turner et al. (2016).

Fig. 9– Modelling contamination of the mantle source by subduction erosion. a) Mixing lines produced by the contamination of the Villarrica mantle source by SVZ crustal material introduced by subduction erosion. The isotopic composition of the Villarrica mantle source was taken from the average composition of primitive Villarrica samples (as Sr and Nd isotopes are not fractionated by melting), and the trace element composition of the metasomatized Villarrica mantle source was taken to be that which, following melting, produces the best model fit for Villarrica in Fig. 8. Only a small percentage of mixing lines pass near Don Casimiro-Maipo. b-c) Trace element and isotopic signatures following melting at F=0.056, P=33 kbar of the mixed mantle compositions that produce isotopic ratios close to Don Casimiro-Maipo (red lines in a), and have Eu/Eu*>0.9. None of these melts recreate Sr, Ba and $^{87}Sr/^{86}Sr$ systematics at Don Casimiro-Maipo. Error bars show 1σ of primitive samples at Don Casimiro-Maipo and Villarrica based on 5 and 3 analyses respectively.

Fig. 10- Variation in rear-arc slab inputs. a) Mixing lines for slab sensitive ratios following the progressive addition of slab melts (20% sediment, 80% AOC) to a depleted and enriched (80% EM1 enrichment) rear-arc mantle source (F=0.02, melting at 33 kbars). The orange wedge reflects progressive mixing of 10% slab (with ODP1232± 1σ) into a mantle source with 0% EM1 enrichment, and the green wedge reflects mixing of 17% slab (with ODP1232± 1σ) into a mantle source with 80% EM1 enrichment. Rear-arc trace element ratios follow these mixing lines remarkably closely. The small amount of scatter away from these modelled trajectories likely reflects variable conditions of melting along the rear-arc. b) Trace element ratios sensitive to slab additions versus trench distance. MORB-like ratios (blue histogram; Gale et al., 2013) start to appear at distances greater than 425 km. Remarkably high, arc-like ratios (black histogram shows primitive samples from the SVZ arc-front; Turner et al. 2016) are seen up to 600 km from the trench, with large scatter in ratios at large trench distances, contrary to the narrow range of observed isotopes.

Fig. 11 –Isotopic compositions of inferred SCLM melts across South America (approximate locations on Fig. 2a). These clearly extend the array that passes from DMM/DAM through the arc-front and rear-arc, to Don Casimiro-Maipo. The field produced by contaminating the Villarrica mantle source with crustal lithologies (Fig. 9a) is overlain (grey), along with the fields for EM1 and EM2-type ocean island basalts (see Fig. 3). Crustal contamination follows a much shallower trajectory than SCLM melts, and is significantly broader than the SCLM field. Southern Rift Mesozoic metabasites were erupted just north of the NSVZ (Lucassen et al., 2002). Craton-edge alkaline melts represent alkaline volcanics erupted on the edges of the Sao Fransisco craton and the Rio Apa-Luis Alves craton on the east coast of South America (Gibson et al., 1995; 2005; Carlson et al., 1996). Santo Domingo Carboniferous granitoids are from the Santo Domingo Complex of the

Coastal Batholith (Parada et al., 1999). These three suites are suggested to have sampled M-SCLM. The green and blue lines show a recycling model in which low-degree melts are extracted from the depleted mantle (Salters and Stracke, 2004) and then aged for up to 2 Ga using the parameters from Stracke et al. (2003; see Turner et al., 2017). A model with F=0.003-0.008 encapsulates the range of isotopic compositions observed in SCLM melts.

Fig. 12- Schematic diagrams showing two possible explanations for the isotopic enrichment minimum and its relationship to tectonic features. a) A Permian suture zone corresponds with an absence of M-SCLM. b) A vertical and horizontal slab tear at ~39˚S may allow depleted Pacific MORB mantle to upwell, and dilute the EM1-type enrichment in the sub-arc mantle located above the tear. As the proportion of depleted Pacific MORB mantle declines northwards and southwards, isotopic signatures become more enriched. Upper plate geometry adapted from box model of Søager et al. (2015b), pp. 1414.

Fig. 13 – Schematic diagrams of rear-arc slab supply. a) Traditional model of slab supply, with buoyant rise of slab fluids to the rear-arc from a slab melting at higher pressure and temperature than that supplying the arc-front. The composition of these fluids should change with increasing trench distance, as the depth to the slab increases. Additionally, at large trench distances, very little to no slab supply would be expected, due to the exhaustion of hydrous phases. b) Proposed model of this study, inspired by Cagnioncle et al. (2007), Wilson et al. (2014) and Cerpa et al. (2017). Down dragging of fluids released at arc-front depths explains the similar composition of arc-front and rear-arc slab supply.

Fig. 14 –A unified model for the SVZ can account for the different trajectories of arc-front and rear-arc samples. a-c) Trace element and isotopic plots showing rear-arc, and filtered SVZ arc-front samples (Eu/Eu*<0.9), along with the composition of the two mantle components used in this study (BAM, EM1), Gough basalts, and the compositional field of MORB (Gale et al., 2013). The composition of mafic enclaves from Longaví are overlain to demonstrate the amount of variability that can be generated from the subducting slab (see d). The unit vectors in a)-c) indicate how varying ambient mantle enrichment, F, and slab components alter the composition of the Baseline Andean Mantle (BAM). Melting trajectories from the model described in section 4.2 are shown in a) and b) to demonstrate the fractionation of certain trace element ratios by the low melt extents that likely dominate the rear-arc. Søager et al. (2013; 2015a) suggest that the offset trajectory of the SVZ arc-front and rear-arc in the cross plots in a)-c) are produced by LCC assimilation. However, varying degrees of EM1 enrichment, variable slab fluxes and variable melt extents can easily account for the offsets between these trajectories. d) Large variations in Ba/Th within arc-front and rear-arc lavas can be accounted for by variable slab additions. For example, mafic enclaves from Longaví

volcano show Ba/Th ratios up to ~500, which have been attributed to the subduction of the Mocho fracture zone beneath this centre (Rodríguez et al., 2007).

References

Baasner, A., Médard, E., Laporte, D. and Hoffer, G., 2016. Partial melting of garnet lherzolite with water and carbon dioxide at 3 GPa using a new melt extraction technique: implications for intraplate magmatism. *Contributions to Mineralogy and Petrology*, **171(5)**, p.45.

Baggerman, T.D. and DeBari, S.M., 2011. The generation of a diverse suite of Late Pleistocene and Holocene basalt through dacite lavas from the northern Cascade arc at Mount Baker, Washington. *Contributions to Mineralogy and Petrology*, *161*(1), pp.75-99.

Boyet, M., Doucelance, R., Israel, C., Bonnand, P., Auclair, D., Suchorski, K. and Bosq, C., 2019. New constraints on the origin of the EM-1 component revealed by the measurement of the La-Ce isotope systematics in Gough Island lavas. *Geochemistry, Geophysics, Geosystems*.

Burd, A.I., Booker, J.R., Mackie, R., Favetto, A. and Pomposiello, M.C., 2014. Three-dimensional electrical conductivity in the mantle beneath the Payun Matru volcanic field in the Andean backarc of Argentina near 36.5° S: evidence for decapitation of a mantle plume by resurgent upper mantle shear during slab steepening. *Geophysical Journal International*, **198**, pp. 812–827.

Cagnioncle, A.M., E. Parmentier, and L. T. Elkins-Tanton., 2007. Effect of solid flow above a subducting slab on water distribution and melting at convergent plate boundaries*. Journal of Geophysical Research*, **112 (B9),** B09402.

Carlson, R.W., Esperanca, S. and Svisero, D.P., 1996. Chemical and Os isotopic study of Cretaceous potassic rocks from southern Brazil. *Contributions to Mineralogy and Petrology*, **125(4)**, pp.393-405.

Carter, L.B., Skora, S., Blundy, J.D., De Hoog, J.C.M. and Elliott, T., 2015. An experimental study of trace element fluxes from subducted oceanic crust. *Journal of Petrology*, **56(8)**, pp.1585-1606.

Cerpa, N.G., Wada, I. and Wilson, C., 2017. Fluid migration in the mantle wedge: Influence of mineral grain size and mantle compaction. *Journal of Geophysical Research: Solid Earth*, **122**, pp. 6247-6268. doi:10.1002/2017JB014046.

Chapman, J.B., Ducea, M.N., DeCelles, P.G. and Profeta, L., 2015. Tracking changes in crustal thickness during orogenic evolution with Sr/Y: An example from the North American Cordillera. *Geology*, **43(10)**, pp.919-922.

Charrier, R., 1979. Los Volcanes Andres y Don Casimiro: Dos centros descubiertos en los Andes entre 34° S Y 34° S 45' Latitud Sur. *Revista Geologica de Chile*, **8**, pp. 79–85.

Chiaradia, M., 2015. Crustal thickness control on Sr/Y signatures of recent arc magmas: an Earth scale perspective. *Scientific reports*, **5**, 8115.

Conrey, R., Grunder, A. and Schmidt, M., 2004. *SOTA Field Trip Guide: State of the Cascade Arc: Stratocone Persistence, Mafic Lava Shields, and Pyroclastic Volcanism Associated with Intra-arc Rift Propagation*. State of Oregon, Department of Geology and Mineral Industries.

Cruz-Uribe, A.M., Marschall, H.R., Gaetani, G.A. and Le Roux, V., 2018. Generation of alkaline magmas in subduction zones by partial melting of mélange diapirs—An experimental study. *Geology*, **46(4)**, pp.343-346.

Davidson, J., Turner, S., Handley, H., Macpherson, C. and Dosseto, A., 2007. Amphibole “sponge” in arc crust?. *Geology*, *35*(9), pp.787-790.

DePaolo, D.J., 1981. Trace element and isotopic effects of combined wallrock assimilation and fractional crystallization. *Earth and Planetary Science Letters*, **53(2)**, pp.189-202.

Dungan, M.A., Wulff, A. and Thompson, R., 2001. Eruptive stratigraphy of the Tatara–San Pedro complex, 36 S, Southern Volcanic Zone, Chilean Andes: reconstruction method and implications for magma evolution at long-lived arc volcanic centers. *Journal of Petrology*, **42(3)**, pp.555-626.

Ewart, A. and Hawkesworth, C.J., 1987. The Pleistocene-Recent Tonga-Kermadec arc lavas: interpretation of new isotopic and rare earth data in terms of a depleted mantle source model. *Journal of Petrology*, **28(3)**, pp.495-530.

Farner, M.J. and Lee, C.T.A., 2017. Effects of crustal thickness on magmatic differentiation in subduction zone volcanism: A global study. *Earth and Planetary Science Letters*, **470**, pp.96-107.

Folguera, A., Naranjo, J.A., Orihashi, Y., Sumino, H., Nagao, K., Polanco, E. and Ramos, V.A., 2009. Retroarc volcanism in the northern San Rafael Block (34–35 30 S), southern Central Andes: Occurrence, age, and tectonic setting. *Journal of Volcanology and Geothermal Research*, **186(3)**, pp. 169-185.

Forni, F., Degruyter, W., Bachmann, O., De Astis, G. and Mollo, S., 2018. Long-term magmatic evolution reveals the beginning of a new caldera cycle at Campi Flegrei. *Science Advances*, *4*(11), eaat9401, DOI: 10.1126/sciadv.aat9401

Futa, K. and Stern, C.R., 1988. Sr and Nd isotopic and trace element compositions of Quaternary volcanic centers of the southern Andes. *Earth and Planetary Science Letters***, 88(3-4)**, pp.253-262.

Gale, A., Dalton, C. A., Langmuir, C. H., Su, Y. and Schilling, J. G., 2013. The Mean Composition of Ocean Ridge Basalts*. Geochemistry, Geophysics, Geosystems*, **14(3)**, pp. 489–518.

Gibson, S. A., Thompson, R. N., Day, J. A., Humphris, S. E. and Dickin, A. P., 2005. Melt-generation processes associated with the Tristan mantle plume: Constraints on the origin of EM-1. *Earth and Planetary Science Letters*, **237(3–4)**, pp. 744–767.

Gibson, S. A., Thompson, R. N., Leonardos, O. H., Dickin, A. P., Mitchell, J. G., Paranaiba, A. and Province, I., 1995. The Late Cretaceous Impact of the Trindade Mantle Plume : Evidence from Magmatism in SE Brazil. *Journal of Petrology***, 36 (1)**, pp. 189-229.

Gudnason, J., Holm, P.M., Søager, N. and Llambías, E.J., 2012. Geochronology of the late Pliocene to recent volcanic activity in the Payenia back-arc volcanic province, Mendoza Argentina. *Journal of South American Earth Sciences*, *37*, pp.191-201.

Hermann, J. and Rubatto, D., 2009. Accessory phase control on the trace element signature of sediment melts in subduction zones. *Chemical Geology*, **265(3–4)**, pp. 512–526.

Hermann, J. and Spandler, C.J., 2007. Sediment melts at sub-arc depths: an experimental study. *Journal of Petrology*, **49(4)**, pp.717-740.

Hickey, R.L., Frey, F.A., Gerlach, D.C. and Lopez-Escobar, L., 1986. Multiple sources for basaltic arc rocks from the southern volcanic zone of the Andes (34–41 S): trace element and isotopic evidence for contributions from subducted oceanic crust, mantle, and continental crust. *Journal of Geophysical Research: Solid Earth*, **91(B6)**, pp.5963-5983.

Hickey-Vargas, R., Roa, H.M., Escobar, L.L. and Frey, F.A., 1989. Geochemical variations in Andean basaltic and silicic lavas from the Villarrica-Lanin volcanic chain (39.5 S): an evaluation of source heterogeneity, fractional crystallization and crustal assimilation. *Contributions to Mineralogy and Petrology*, ***103*(3),** pp.361-386.

Hickey-Vargas, R., Holbik, S., Tormey, D., Frey, F.A. and Roa, H.M., 2016. Basaltic rocks from the Andean Southern Volcanic Zone: Insights from the comparison of along-strike and small-scale geochemical variations and their sources. *Lithos*, **258**, pp.115-132.

Hildreth, W. and Moorbath, S., 1988. Crustal contribution to arc magmatism in the Andes of Central Chile. *Contributions to Mineralogy and Petrology*, **98**, pp. 455–489.

Hildreth, W. and Moorbath, S., 1991. Reply to Comment on "Crustal contributions to arc magmatism in the Andes of Central Chile" by W. Hildreth and S. Moorbath. *Contributions to Mineralogy and Petrology***, 108(1)**, pp. 247-252.

Hirai, Y., Yoshida, T., Okamura, S., Tamura, Y., Sakamoto, I. and Shinjo, R., 2018. Breakdown of residual zircon in the Izu arc subducting slab during backarc rifting. *Geology*, **46(4)**, pp.371-374.

Hochstaedter, A., Gill, J., Peters, R., Broughton, P., Holden, P. and Taylor, B., 2001. Across-arc geochemical trends in the Izu-Bonin arc: Contributions from the subducting slab. *Geochemistry, Geophysics, Geosystems*, **2(7)**, 2000GC000105.

Holm, P.M., Søager, N., Alfastsen, M. and Bertotto, G.W., 2016. Subduction zone mantle enrichment by fluids and Zr–Hf-depleted crustal melts as indicated by backarc basalts of the Southern Volcanic Zone, Argentina. *Lithos*, **262**, pp. 145-152.

Holm, P.M., Søager, N., Dyhr, C.T. and Nielsen, M.R., 2014. Enrichments of the mantle sources beneath the Southern Volcanic Zone (Andes) by fluids and melts derived from abraded upper continental crust. *Contributions to Mineralogy and Petrology*, **167(5),** 1004, https://doi.org/10.1007/s00410-014-1004-8

Jacques, G., Hoernle, K., Gill, J., Hauff, F., Wehrmann, H., Garbe-Schönberg, D., van den Bogaard, P., Bindeman, I. and Lara, L. E., 2013. Across-arc geochemical variations in the Southern Volcanic Zone, Chile (34.5-38.0° S): Constraints on mantle wedge and slab input compositions. *Geochimica et Cosmochimica Acta*, **123**, pp. 218–243.

Jacques, G., Hoernle, K., Gill, J., Wehrmann, H., Bindeman, I. and Lara, L. E., 2014. Geochemical variations in the Central Southern Volcanic Zone, Chile (38 – 43 ° S): The role of fluids in generating arc magmas. *Chemical Geology*, **371**, pp. 27–45.

Johnson, M. C., and Plank, T., 1999. Dehydration and melting experiments constrain the fate of subducted sediments. *Geochemistry, Geophysics, Geosystems***, 1(1)**, 1007, doi:10.1029/1999GC000014.

Karlstrom, L., Lee, C.T. and Manga, M., 2014. The role of magmatically driven lithospheric thickening on arc front migration. *Geochemistry, Geophysics, Geosystems***, 15(6)**, pp.2655-2675.

Kay S. M., Burns, W. M., Copeland, P., & Mancilla, O.(2006). Upper Cretaceous to Holocene magmatism and evidence for transient Miocene shallowing of the Andean subduction zone under the northern Neuquén Basin. *Special papers - geological society of America*, ***407*****,** 19

Kay, S.M., Orrell, S. and Abbruzzi, J.M., 1996. Zircon and whole rock Nd-Pb isotopic evidence for a Grenville age and a Laurentian origin for the basement of the Precordillera in Argentina. *The Journal of Geology*, *104*(6), pp.637-648.

Kay, S.M. and Copeland, P., 2006. Early to middle Miocene backarc magmas of the Neuquén Basin: Geochemical consequences of slab shallowing and the westward drift of South America. *Geological Society of America Special Papers***, 407(9)**, pp. 185–213.

Kay, S.M., Godoy, E. and Kurtz, A., 2005. Episodic arc migration, crustal thickening, subduction erosion, and magmatism in the south-central Andes. *Bulletin of the Geological Society of America*, **117(1–2)**, pp. 67–88.

Kay, S.M., Jones, H.A. and Kay, R.W., 2013. Origin of Tertiary to Recent EM1 and subduction-like chemical and isotopic signatures in Auca Mahuida region (37-38S) and other Patagonian plateau lavas. *Contributions to Mineralogy and Petrology*, **166(1)**, pp. 165–192.

Kelley, K.A., Plank, T., Ludden, J. and Staudigel, H., 2003. Composition of altered oceanic crust at ODP Sites 801 and 1149. *Geochemistry, Geophysics, Geosystems*, *4*(6).

Kessel, R., Schmidt, M.W., Ulmer, P. and Pettke, T., 2005. Trace element signature of subduction-zone fluids, melts and supercritical liquids at 120–180 km depth. *Nature*, **437(7059)**, pp.724-727.

Klaver, M., Davies, G.R. and Vroon, P.Z., 2016. Subslab mantle of African provenance infiltrating the Aegean mantle wedge. *Geology*, **44(5)**, pp. 367-370.

Knott, T.R., Branney, M.J., Reichow, M.K., Finn, D.R., Coe, R.S., Storey, M., Barfod, D. and McCurry, M., 2016. Mid-Miocene record of large-scale Snake River–type explosive volcanism and associated subsidence on the Yellowstone hotspot track: The Cassia Formation of Idaho, USA. *Bulletin*, *128*(7-8), pp.1121-1146.

Leeman, W.P., 1983. The influence of crustal structure on compositions of subduction-related magmas. *Journal of Volcanology and Geothermal Research*, **18(1-4),** pp.561-588.

Lee, C.T.A., Lee, T.C. and Wu, C.T., 2014. Modeling the compositional evolution of recharging, evacuating, and fractionating (REFC) magma chambers: Implications for differentiation of arc magmas. *Geochimica et Cosmochimica Acta*, *143*, pp.8-22.

Lopez-Escobar, L., Frey, F.A. and Vergara, M., 1977. Andesites and high-alumina basalts from the central-south Chile High Andes: geochemical evidence bearing on their petrogenesis. *Contributions to Mineralogy and Petrology*, **63(3)**, pp.199-228.

Lucassen, F., Becchio, R., Harmon, R., Kasemann, S., Franz, G., Trumbull, R., Wilke, H., Romer, R. L. and Dulski, P., 2001. Composition and density model of the continental crust at an active continental margin — the Central Andes between 21 ° S and 27 ° S. *Tectonophysics,* **341(1)**, pp. 195–223.

Lucassen, F., Escayola, Æ. M., Romer, A. R. L., Kerstin, V. Æ. and Gerhard, K. Æ., 2002. Isotopic composition of Late Mesozoic basic and ultrabasic rocks from the Andes (23 – 32 ° S) – implications for the Andean mantle. *Contributions to Mineralogy and Petrology*, **143(3)** pp. 336–349.

Lucassen, F., Trumbull, R., Franz, G., Creixell, C., Vásquez, P., Romer, R. L. and Figueroa, O., 2004. Distinguishing crustal recycling and juvenile additions at active continental margins: The Paleozoic to recent compositional evolution of the Chilean Pacific margin (36-41° S). *Journal of South American Earth Sciences*, **17(2)**, pp. 103–119.

MacDougall, J.G., Jadamec, M.A. and Fischer, K.M., 2017. The zone of influence of the subducting slab in the asthenospheric mantle. *Journal of Geophysical Research: Solid Earth*, *122*(8), pp.6599-6624.

McDonough, W.F. and Sun, S.S., 1995. The composition of the Earth. *Chemical Geology*, **120**, pp. 223-253.

McKenzie, D.. and O'Nions, R.K., 1995. The source regions of ocean island basalts. *Journal of Petrology*, **36(1)**, pp.133-159.

Morgado, E., Parada, M.A., Contreras, C., Castruccio, A., Gutiérrez, F. and McGee, L.E., 2015. Contrasting records from mantle to surface of Holocene lavas of two nearby arc volcanic complexes: Caburgua-Huelemolle Small Eruptive Centers and Villarrica Volcano, Southern Chile. *Journal of Volcanology and Geothermal Research*, *306*, pp.1-16.

Orozco, G., Garces, F., Jara, G., and Lara, L.E., 2015. Nuevos antecedentes para la geología del complejo volcánico Maipo-Diamante, Andes del Sur. Congreso Geologico Chileno, La Serena, Octubre 2015. (abstract – accessed http://biblioteca.sernageomin.cl/opac/DataFiles/14905_v3_pp_218_221.pdf, 13th January, 2018).

Pallares, C., Quidelleur, X., Gillot, P.Y., Kluska, J.M., Tchilinguirian, P. and Sarda, P., 2016. The temporal evolution of back-arc magmas from the Auca Mahuida shield volcano (Payenia Volcanic Province, Argentina). *Journal of Volcanology and Geothermal Research*, *323*, pp.19-37.

Parada, M.A., Nyström, J.O. and Levi, B.., 1999. Multiple sources for the Coastal Batholith of central Chile (31–34 S): geochemical and Sr–Nd isotopic evidence and tectonic implications. *Lithos*, **46(3)**, pp.505-521.

Patino, L.C., Carr, M.J. and Feigenson, M.D., 2000. Local and regional variations in Central American arc lavas controlled by variations in subducted sediment input. *Contributions to Mineralogy and Petrology*, *138*(3), pp.265-283.

Pearce, J.A., Kempton, P.D. and Gill, J.B., 2007. Hf–Nd evidence for the origin and distribution of mantle domains in the SW Pacific. *Earth and Planetary Science Letters*, **260(1)**, pp.98-114.

Pesicek, J. D., Engdahl, E. R., Thurber, C. H., Deshon, H. R. and Lange, D., 2012. Mantle subducting slab structure in the region of the 2010 M8.8 Maule earthquake (30-40° S), Chile. *Geophysical Journal International*, **191(1)**, pp. 317–324.

Plank, T., Kelley, K.A., Zimmer, M.M., Hauri, E.H. and Wallace, P.J., 2013. Why do mafic arc magmas contain~ 4 wt% water on average?. *Earth and Planetary Science Letters*, *364*, pp.168-179.

Plank, T. and Langmuir, C.H., 1988. An evaluation of the global variations in the major element chemistry of arc basalts. *Earth and Planetary Science Letters*, **90**, pp. 349–370.

Plank, T., 2005. Constraints from thorium/lanthanum on sediment recycling at subduction zones and the evolution of the continents. *Journal of Petrology*, **46(5)**, pp.921-944.

Profeta, L., Ducea, M.N., Chapman, J.B., Paterson, S.R., Gonzales, S.M.H., Kirsch, M., Petrescu, L. and DeCelles, P.G., 2015. Quantifying crustal thickness over time in magmatic arcs. *Scientific Reports*, **5**, 17786, https://doi.org/10.1038/srep17786.

Ramos, V.A., 2010. The Grenville-age basement of the Andes, *Journal of South American Earth Sciences*, **29**, pp. 77–91.

Rapalini, A.E., de Luchi, M.G.L., Dopico, C.M., Klinger, F.G.L., Giménez, M.E., Martínez, P., 2010. Did Patagonia collide with Gondwana in the Late Paleozoic? Some insights from a multidisciplinary study of magmatic units of the North Patagonian Massif. *Geologica Acta*, **8**, 349-371.

Rodrĺguez, C., Sellés, D., Dungan, M., Langmuir, C. and Leeman, W., 2007. Adakitic dacites formed by intracrustal crystal fractionation of water-rich parent magmas at Nevado de Longaví volcano (36· 2 S; Andean Southern Volcanic Zone, Central Chile). *Journal of Petrology*, *48*(11), pp.2033-2061.

Rogers, G. and Hawkesworth, C.J., 1989. A geochemical traverse across the North Chilean Andes: evidence for crust generation from the mantle wedge. *Earth and Planetary Science Letters*, **91**, pp. 271-285.

Rudnick, R.L. and Gao, S., 2003. Composition of the continental crust. In: *Treatise on Geochemistry: The Crust* (Eds. R. Rudnick), **vol. 3**. Permagon, New York, pp. 1–64.

Ruscitto, D.M., Wallace, P.J., Cooper, L.B. and Plank, T., 2012. Global variations in H2O/Ce: 2. Relationships to arc magma geochemistry and volatile fluxes. *Geochemistry, Geophysics, Geosystems*, **13(3), Q03025, doi:10.1029/2011GC003887.**

Salters, V.J. and Stracke, A., 2004. Composition of the depleted mantle. *Geochemistry, Geophysics, Geosystems***, 5(5)**, Q05004, doi:10.1029/2003GC000597.

Savov, I.P., Ryan, J.G., D'Antonio, M. and Fryer, P., 2007. Shallow slab fluid release across and along the Mariana arc-basin system: Insights from geochemistry of serpentinized peridotites from the Mariana fore arc. *Journal of Geophysical Research: Solid Earth*, **112(B9),** B09205, doi:10.1029/2006JB004749.

Schmidt, M.W. and Jagoutz, O., 2017. The global systematics of primitive arc melts. *Geochemistry, Geophysics, Geosystems*, **18(8)**, pp.2817-2854.

Scott, E.M., Allen, M.B., Macpherson, C.G., McCaffrey, K.J., Davidson, J.P., Saville, C. and Ducea, M.N., 2018. Andean surface uplift constrained by radiogenic isotopes of arc lavas. *Nature Communications*, **9(1)**, 969, doi: 10.1038/s41467-018-03173-4.

Sisson, T.W. and Kelemen, P.B., 2018. Near-solidus melts of MORB+ 4 wt% H 2 O at 0.8–2.8 GPa applied to issues of subduction magmatism and continent formation. *Contributions to Mineralogy and Petrology*, **173(9)**, 70, doi: 10.1007/s00410-018-1494-x.

Sisson, T.W., Salters, V.J.M. and Larson, P.B., 2014. Petrogenesis of Mount Rainier andesite: Magma flux and geologic controls on the contrasting differentiation styles at stratovolcanoes of the southern Washington Cascades. *Bulletin*, *126*(1-2), pp.122-144.

Skora, S. and Blundy, J., 2010. High-pressure hydrous phase relations of radiolarian clay and implications for the involvement of subducted sediment in arc magmatism. *Journal of Petrology*, **51(11)**, pp.2211-2243.

Søager, N. and Holm, P.M., 2013. Melt-peridotite reactions in upwelling eclogite bodies: Constraints from EM1-type alkaline basalts in Payenia, Argentina. *Chemical Geology*, **360–361**, pp. 204–219.

Søager, N., Holm, P.M. and Llambías, E.J., 2013. Payenia volcanic province, southern mendoza, argentina: OIB mantle upwelling in a backarc environment. *Chemical Geology*, **349–350**, pp. 36–53.

Søager, N., Martin, P. and Thirlwall, M.F., 2015a. Sr , Nd , Pb and Hf isotopic constraints on mantle sources and crustal contaminants in the Payenia volcanic province, Argentina. *Lithos*, **212–215**, pp. 368–378.

Søager, N., Portnyagin, M., Hoernle, K., Holm, P. M., Hauff, F. and Garbe-Schanberg, D., 2015b. Olivine major and trace element compositions in Southern Payenia Basalts, Argentina: Evidence for

pyroxenite-peridotite melt mixing in a back-arc setting. *Journal of Petrology*, **56(8)**, pp. 1395–1518.

Spandler, C., Mavrogenes, J. and Hermann, J., 2007. Experimental constraints on element mobility from subducted sediments using high-P synthetic fluid/melt inclusions. *Chemical Geology*, **239(3)**, pp. 228-249.

Sruoga, P., Llambías, E.J., Fauqué, L., Schonwandt, D. and Repol, D.G., 2005. Volcanological and geochemical evolution of the Diamante Caldera–Maipo volcano complex in the southern Andes of Argentina (34 10 S). *Journal of South American Earth Sciences*, **19(4)**, pp. 399-414.

Stern, C.R., 1989. Pliocene to present migration of the volcanic front, Andean Southern Volcanic Zone. *Andean Geology*, **16(2)**, pp.145-162.

Stern, C.R., 2011. Subduction erosion: rates, mechanisms, and its role in arc magmatism and the evolution of the continental crust and mantle. *Gondwana Research*, *20*(2-3), pp.284-308.

Stracke, A., Bizimis, M. and Salters, V.J., 2003. Recycling oceanic crust: Quantitative constraints. *Geochemistry, Geophysics, Geosystems*, **4(3),** 8003. https://doi.org/10.1029/2001GC000223

Syracuse, E. M., van Keken, P. E., Abers, G. A., Suetsugu, D., Bina, C., Inoue, T., Wiens, D. and Jellinek, M., 2010. The global range of subduction zone thermal models, *Physics of the Earth and Planetary Interiors*, **183(1–2)**, pp. 73–90.

Tassara, A. and Echaurren, A., 2012. Anatomy of the Andean subduction zone: Three-dimensional density model upgraded and compared against global-scale models. *Geophysical Journal International*, **189(1)**, pp. 161–168.

Tormey, D., Hickey-Vargas, R., Frey, F., Lopez-Escobar, L., 1991. Recent lavas from the Andean front (32 to 42° S); Interpretations of along-arc compositional variations. *Geological Society of America, Special Paper*, **265**, pp. 57–77.

Turner, S.J. and Langmuir, C.H., 2015a. The global chemical systematics of arc front stratovolcanoes: Evaluating the role of crustal processes. *Earth and Planetary Science Letters*, **422**, pp.182-193.

Turner, S. J., and Langmuir, C. H., 2015b, What processes control the chemical compositions of arc front stratovolcanoes? *Geochemistry, Geophysics, Geosystems*, **16**, pp. 1865–1893.

Turner, S. J., Langmuir, C. H., Katz, R. F., Dungan, M. A. and Escrig, S., 2016. Parental arc magma compositions dominantly controlled by mantle-wedge thermal structure. *Nature Geoscience*, **9**, pp. 772-776.

Turner, S.J., Langmuir, C.H., Dungan, M.A. and Escrig, S., 2017. The importance of mantle wedge heterogeneity to subduction zone magmatism and the origin of EM1. *Earth and Planetary Science Letter*s, **472**, pp.216-228.

Valdenegro, P., Muñoz, M., Yáñez, G., Parada, M.A. and Morata, D., 2019. A model for thermal gradient and heat flow in central Chile: The role of thermal properties. *Journal of South American Earth Sciences*, *91*, pp.88-101.

Völker, D., Kutterolf, S. and Wehrmann, H., 2011. Comparative mass balance of volcanic edifices at the southern volcanic zone of the Andes between 33 S and 46 S. *Journal of Volcanology and Geothermal Research*, **205(3-4)**, pp.114-129.

Völker, D., Geersen, J., Contreras-Reyes, E. and Reichert, C., 2013. Sedimentary fill of the Chile Trench (32–46° S): volumetric distribution and causal factors. *Journal of the Geological Society*, *170*(5), pp.723-736.

Willbold, M. and Stracke, A. 2010. Formation of enriched mantle components by recycling of upper and lower continental crust. *Chemical Geology*, **276(3–4)**, pp. 188–197.

Wilson, C.R., Spiegelman, M., van Keken, P.E. and Hacker, B.R., 2014. Fluid flow in subduction zones: the role of solid rheology and compaction pressure. *Earth and Planetary Science Letters*, **401**, pp. 261–274.

Woodhead, J., Stern, R.J., Pearce, J., Hergt, J., Vervoort, J., 2012. Hf-Nd isotope variation in Mariana Trough basalts: The importance of "ambient mantle" in the interpretation of subduction zone magmas. *Geology*, **40**, pp. 539-542

Workman, R.K. and Hart, S.R., 2005. Major and trace element composition of the depleted MORB mantle (DMM). *Earth and Planetary Science Letters*, **231(1–2)**, pp. 53–72.

Zandt, G. and Humphreys, E., 2008. Toroidal mantle flow around the western US slab window. *Geology*, **36(4)**, pp. 295-298.

Zindler A., and Hart S., 1986. Chemical Geodynamics. *Annual Review of Earth Planetary Sciences*, **14**, pp. 493–571

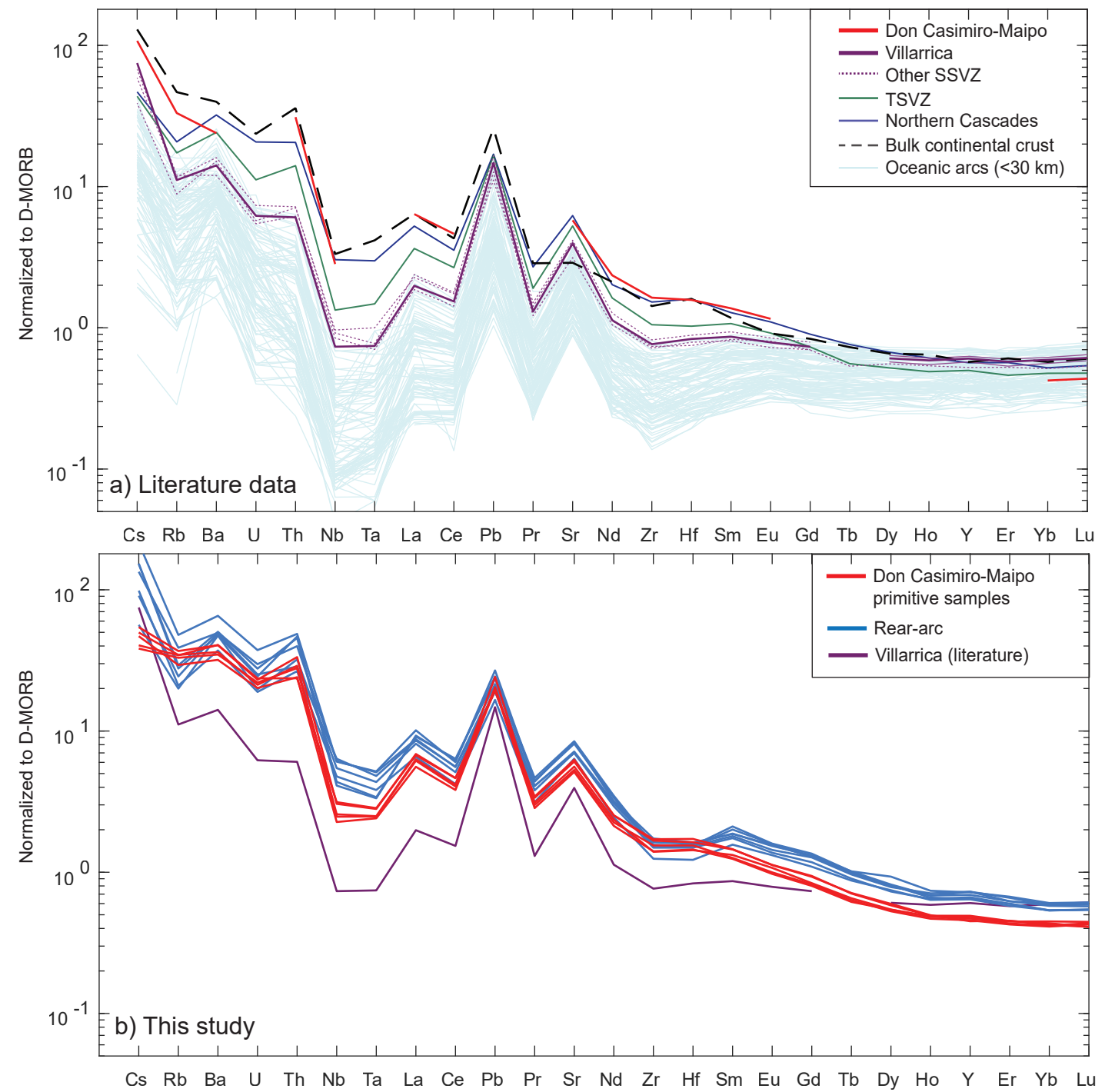
Normalized to D-MORB
Don Casimiro-Maipo
Villarrica
Other SSVZ
TSVZ
Northern Cascades
Bulk continental crust
Oceanic arcs (<30 km)
a) Literature data
Cs Rb Ba U Th Nb Ta La Ce Pb Pr Sr Nd Zr Hf Sm Eu Gd Tb Dy Ho Y Er Yb Lu
Normalized to D-MORB
Don Casimiro-Maipo primitive samples
Rear-arc
Villarrica (literature)
b) This study
Cs Rb Ba U Th Nb Ta La Ce Pb Pr Sr Nd Zr Hf Sm Eu Gd Tb Dy Ho Y Er Yb Lu

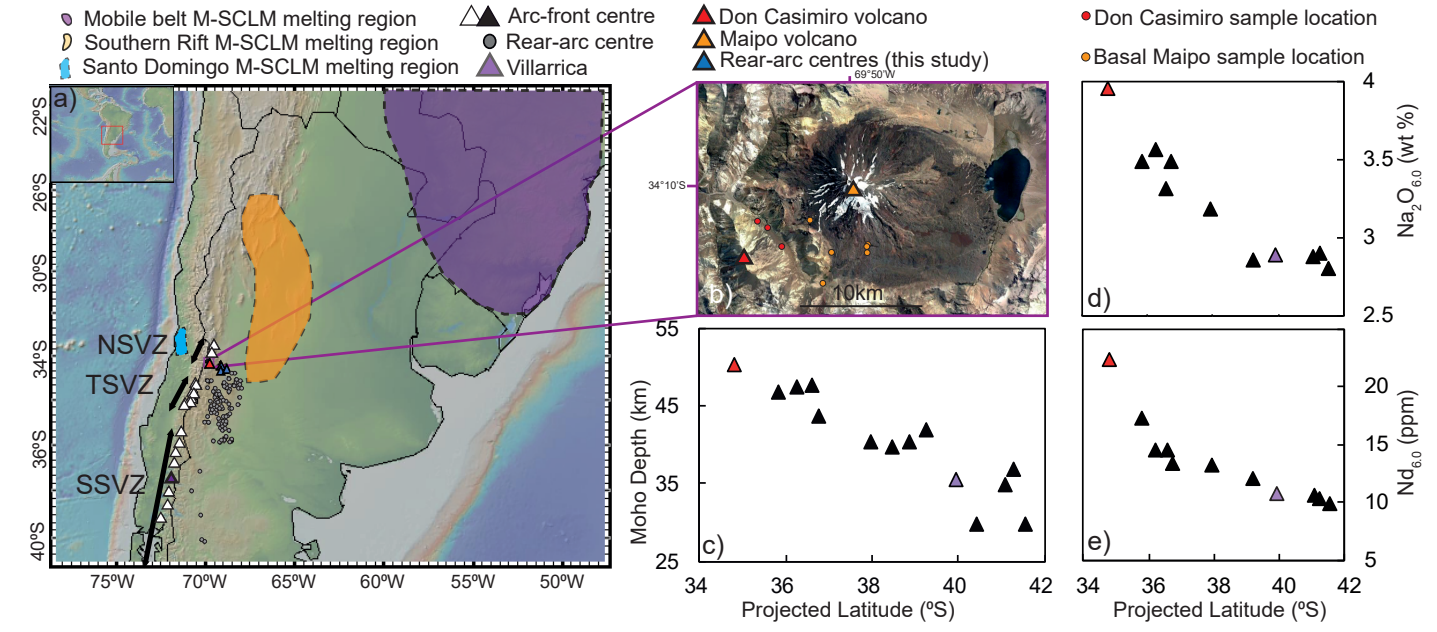
Mobile belt M-SCLM melting region
Southern Rift M-SCLM melting region
Santo Domingo M-SCLM melting region
Arc-front centre
Rear-arc centre
Villarrica
Don Casimiro volcano
Maipo volcano
Rear-arc centres (this study)
Don Casimiro sample location
Basal Maipo sample location
a)
NSVZ
TSVZ
SSVZ
22ºS
26ºS
30ºS
34ºS
36ºS
40ºS
75ºW
70ºW
65ºW
60ºW
55ºW
50ºW
69°50'W
34°10'S
b)
10km
c)
Moho Depth (km)
Projected Latitude (ºS)
d)
$Na_2O_{6.0}$ (wt %)
e)
$Nd_{6.0}$ (ppm)
Projected Latitude (ºS)

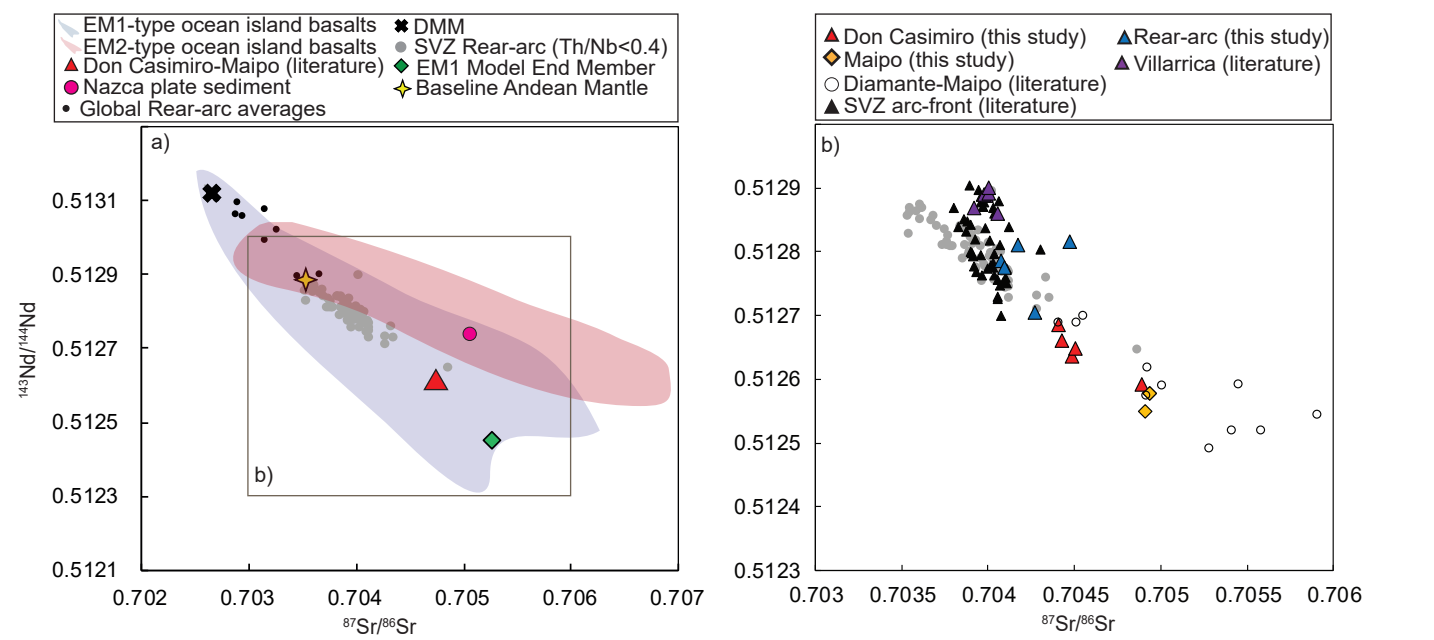
EM1-type ocean island basalts
EM2-type ocean island basalts
Don Casimiro-Maipo (literature)
Nazca plate sediment
Global Rear-arc averages
DMM
SVZ Rear-arc (Th/Nb<0.4)
EM1 Model End Member
Baseline Andean Mantle
a)
b)
0.5131
0.5129
0.5127
0.5125
0.5123
0.5121
143Nd/144Nd
0.702
0.703
0.704
0.705
0.706
0.707
87Sr/86Sr
Don Casimiro (this study)
Maipo (this study)
Diamante-Maipo (literature)
SVZ arc-front (literature)
Rear-arc (this study)
Villarrica (literature)
b)
0.5129
0.5128
0.5127
0.5126
0.5125
0.5124
0.5123
0.703
0.7035
0.704
0.7045
0.705
0.7055
0.706
87Sr/86Sr

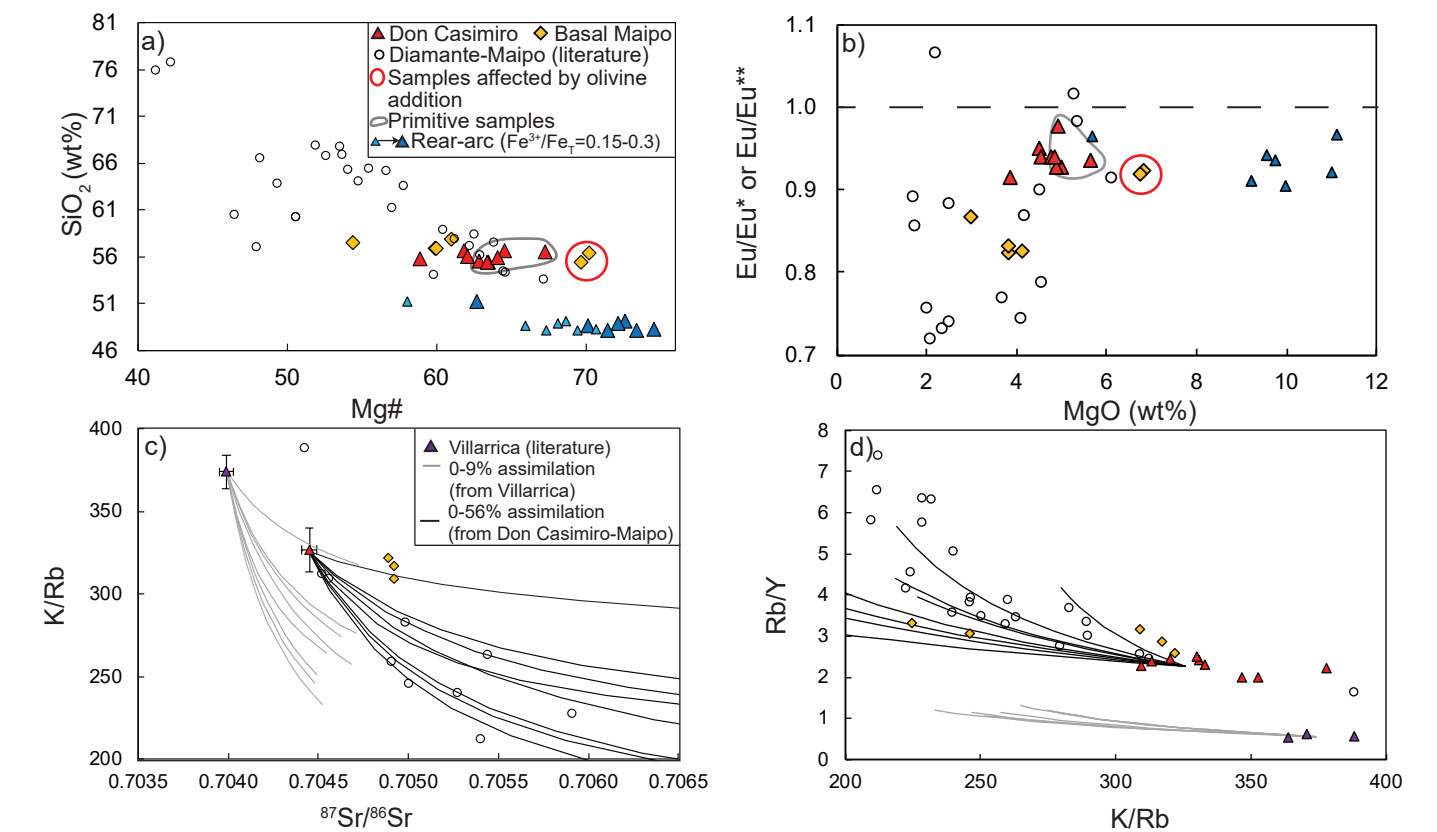
a)
Don Casimiro
Basal Maipo
Diamante-Maipo (literature)
Samples affected by olivine addition
Primitive samples
Rear-arc (Fe3+/FeT=0.15-0.3)
SiO2 (wt%)
Mg#
b)
Eu/Eu* or Eu/Eu**
MgO (wt%)
c)
Villarrica (literature)
0-9% assimilation (from Villarrica)
0-56% assimilation (from Don Casimiro-Maipo)
K/Rb
87Sr/86Sr
d)
Rb/Y
K/Rb

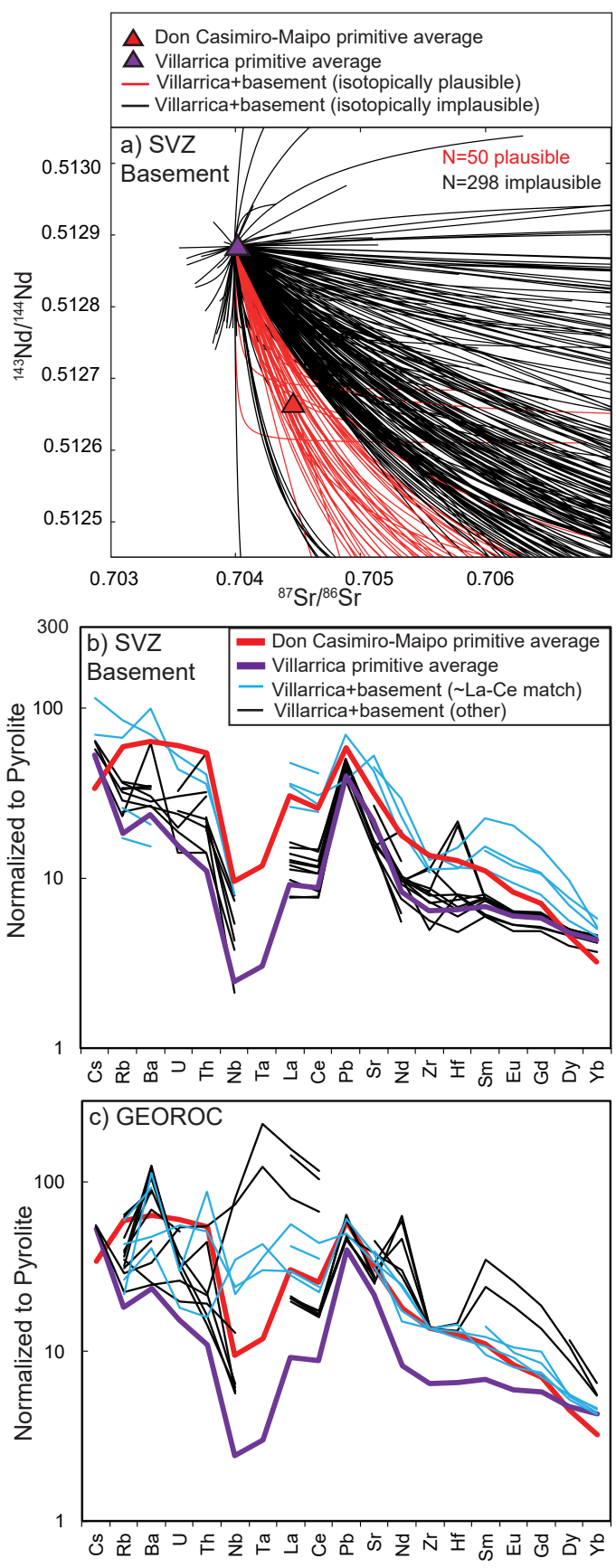
Don Casimiro-Maipo primitive average
Villarrica primitive average
Villarrica+basement (isotopically plausible)
Villarrica+basement (isotopically implausible)
a) SVZ
Basement
N=50 plausible
N=298 implausible
0.5130
0.5129
0.5128
0.5127
0.5126
0.5125
143Nd/144Nd
0.703
0.704
0.705
0.706
87Sr/86Sr
b) SVZ
Basement
Don Casimiro-Maipo primitive average
Villarrica primitive average
Villarrica+basement (~La-Ce match)
Villarrica+basement (other)
300
100
10
1
Normalized to Pyrolite
Cs
Rb
Ba
U
Th
Nb
Ta
La
Ce
Pb
Sr
Nd
Zr
Hf
Sm
Eu
Gd
Dy
Yb
c) GEOROC
100
10
1
Normalized to Pyrolite
Cs
Rb
Ba
U
Th
Nb
Ta
La
Ce
Pb
Sr
Nd
Zr
Hf
Sm
Eu
Gd
Dy
Yb

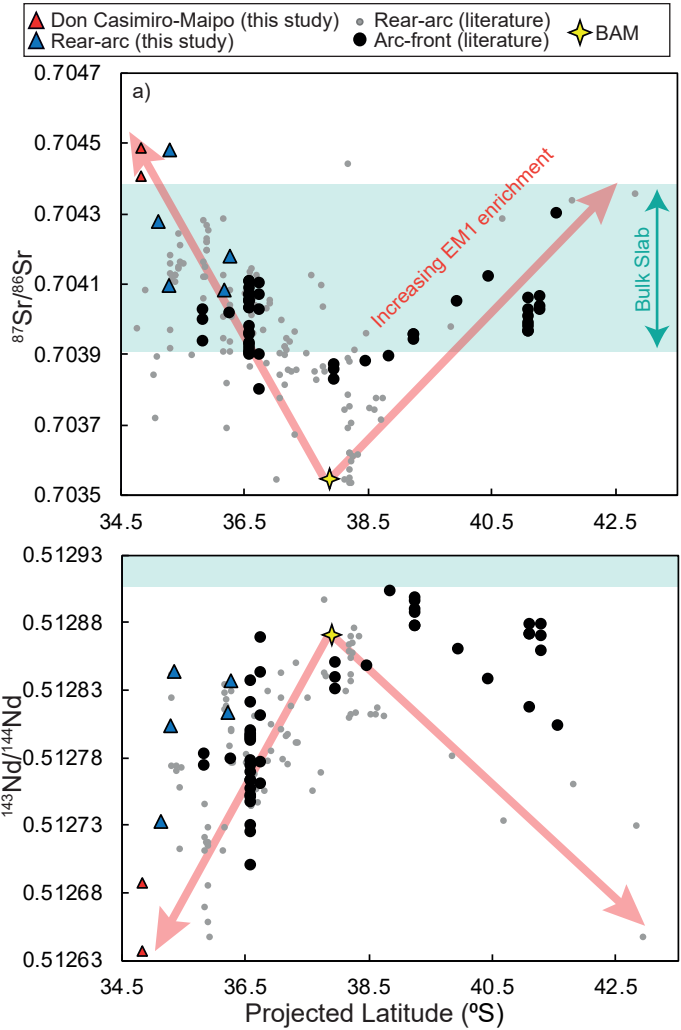
Don Casimiro-Maipo (this study)
Rear-arc (this study)
Rear-arc (literature)
Arc-front (literature)
BAM
a)
$^{87}Sr/^{86}Sr$
0.7047
0.7045
0.7043
0.7041
0.7039
0.7037
0.7035
Increasing EM1 enrichment
Bulk Slab
34.5
36.5
38.5
40.5
42.5
$^{143}Nd/^{144}Nd$
0.51293
0.51288
0.51283
0.51278
0.51273
0.51268
0.51263
Projected Latitude (ºS)

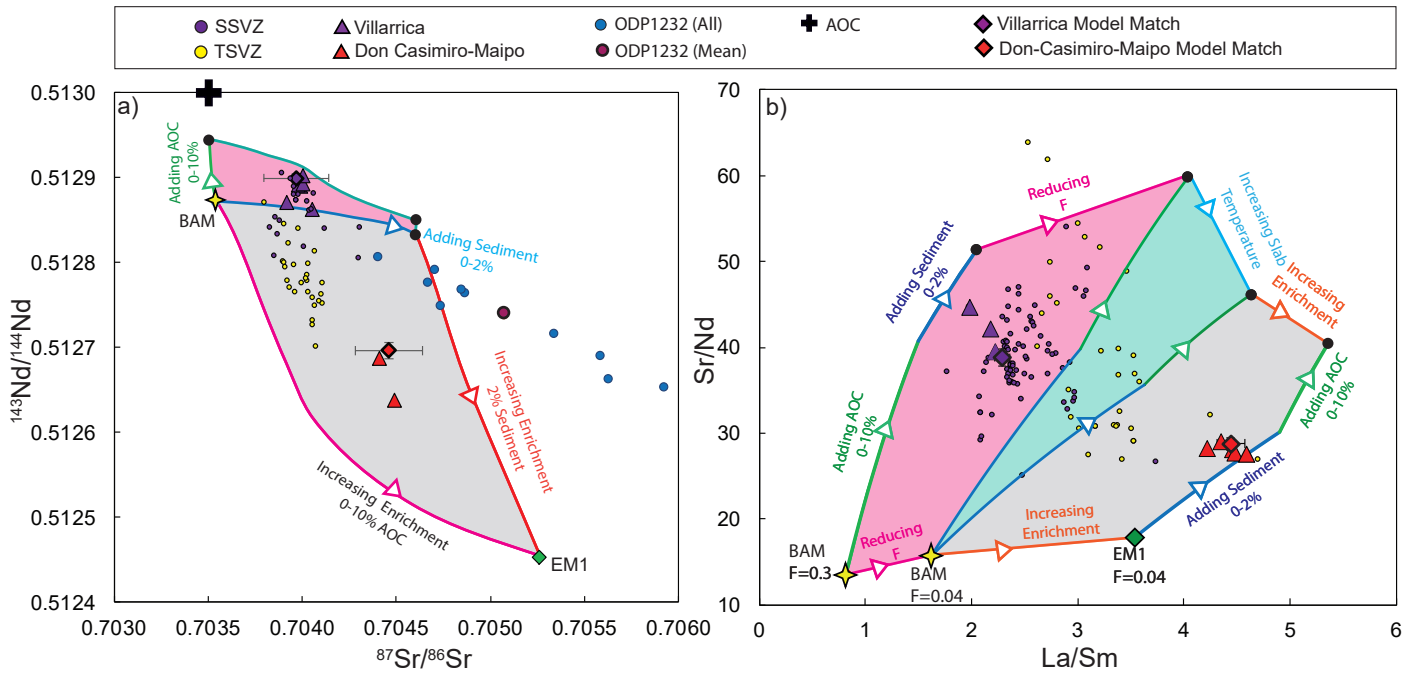
SSVZ
TSVZ
Villarrica
Don Casimiro-Maipo
ODP1232 (All)
ODP1232 (Mean)
AOC
Villarrica Model Match
Don-Casimiro-Maipo Model Match
a)
Adding AOC 0-10%
BAM
Adding Sediment 0-2%
Increasing Enrichment 2% Sediment
Increasing Enrichment 0-10% AOC
EM1
143Nd/144Nd
87Sr/86Sr
0.5130
0.5129
0.5128
0.5127
0.5126
0.5125
0.5124
0.7030
0.7035
0.7040
0.7045
0.7050
0.7055
0.7060
b)
Reducing F
Adding Sediment 0-2%
Increasing Slab Temperature
Increasing Enrichment
Adding AOC 0-10%
Adding AOC 0-10%
Reducing F
BAM F=0.3
BAM F=0.04
Increasing Enrichment
Adding Sediment 0-2%
EM1 F=0.04
Sr/Nd
La/Sm
70
60
50
40
30
20
10
0
1
2
3
4
5
6

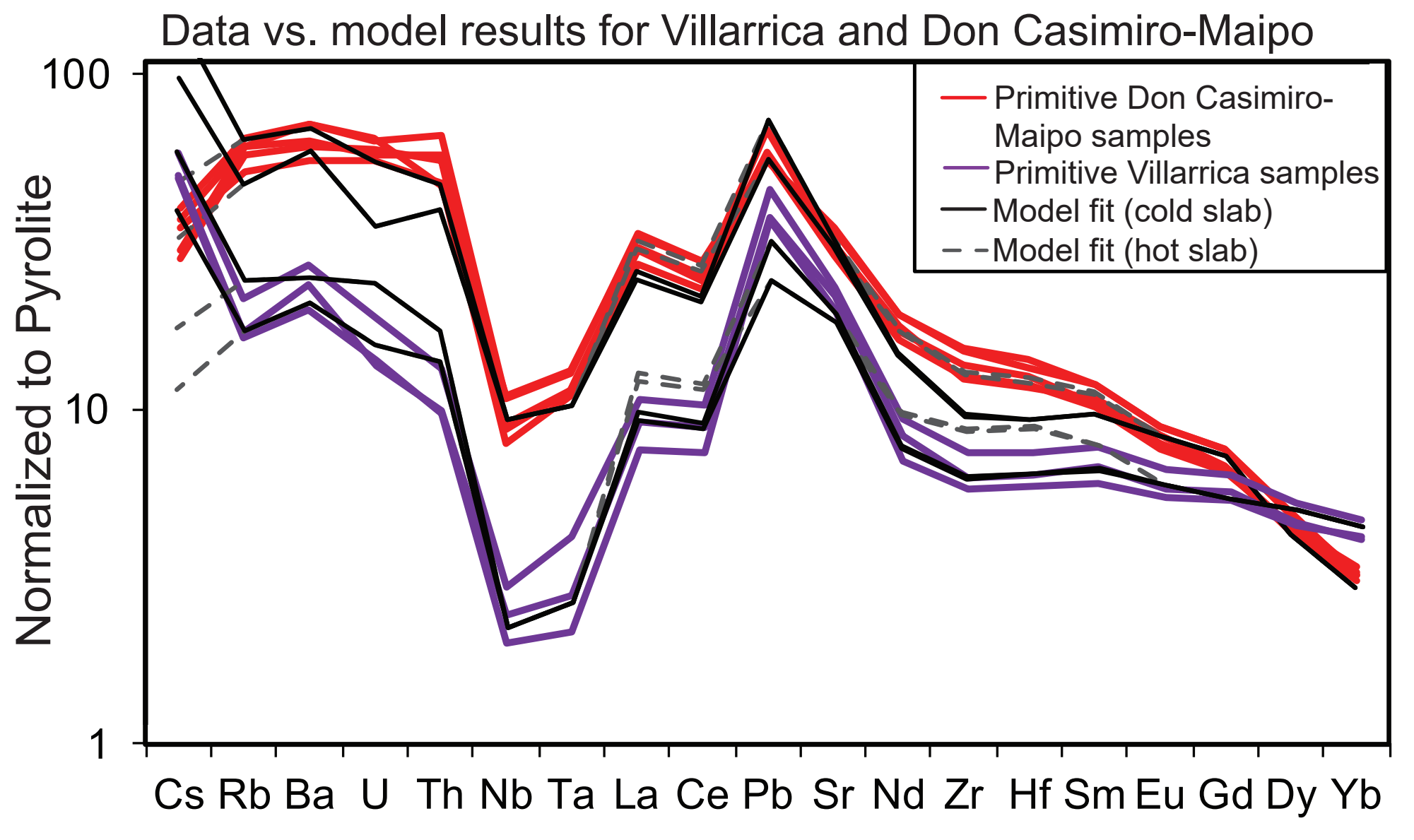
Data vs. model results for Villarrica and Don Casimiro-Maipo
Normalized to Pyrolite
100
10
1
Cs Rb Ba U Th Nb Ta La Ce Pb Sr Nd Zr Hf Sm Eu Gd Dy Yb
Primitive Don Casimiro-Maipo samples
Primitive Villarrica samples
Model fit (cold slab)
Model fit (hot slab)

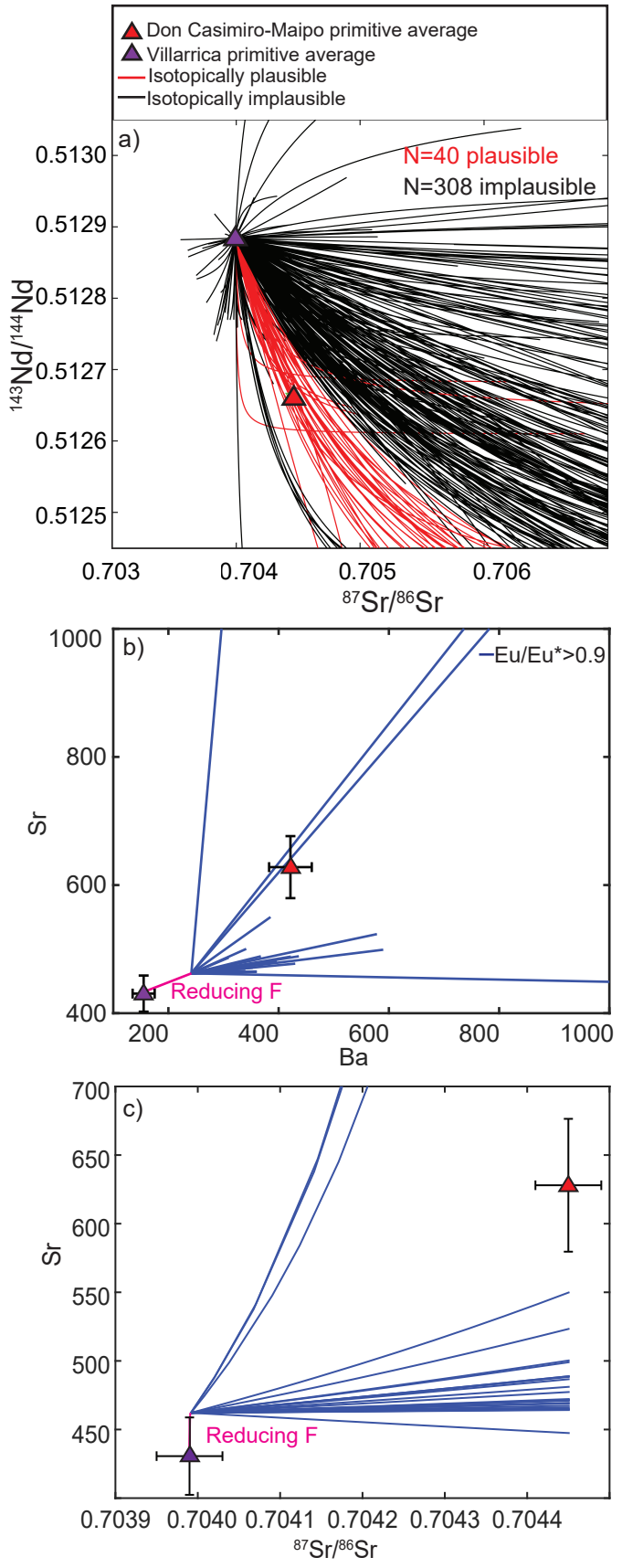
Don Casimiro-Maipo primitive average
Villarrica primitive average
Isotopically plausible
Isotopically implausible
a)
N=40 plausible
N=308 implausible
0.5130
0.5129
0.5128
0.5127
0.5126
0.5125
143Nd/144Nd
0.703
0.704
0.705
0.706
87Sr/86Sr
b)
Eu/Eu*>0.9
1000
800
600
400
Sr
Reducing F
200
400
600
800
1000
Ba
c)
700
650
600
550
500
450
Sr
Reducing F
0.7039
0.7040
0.7041
0.7042
0.7043
0.7044
87Sr/86Sr

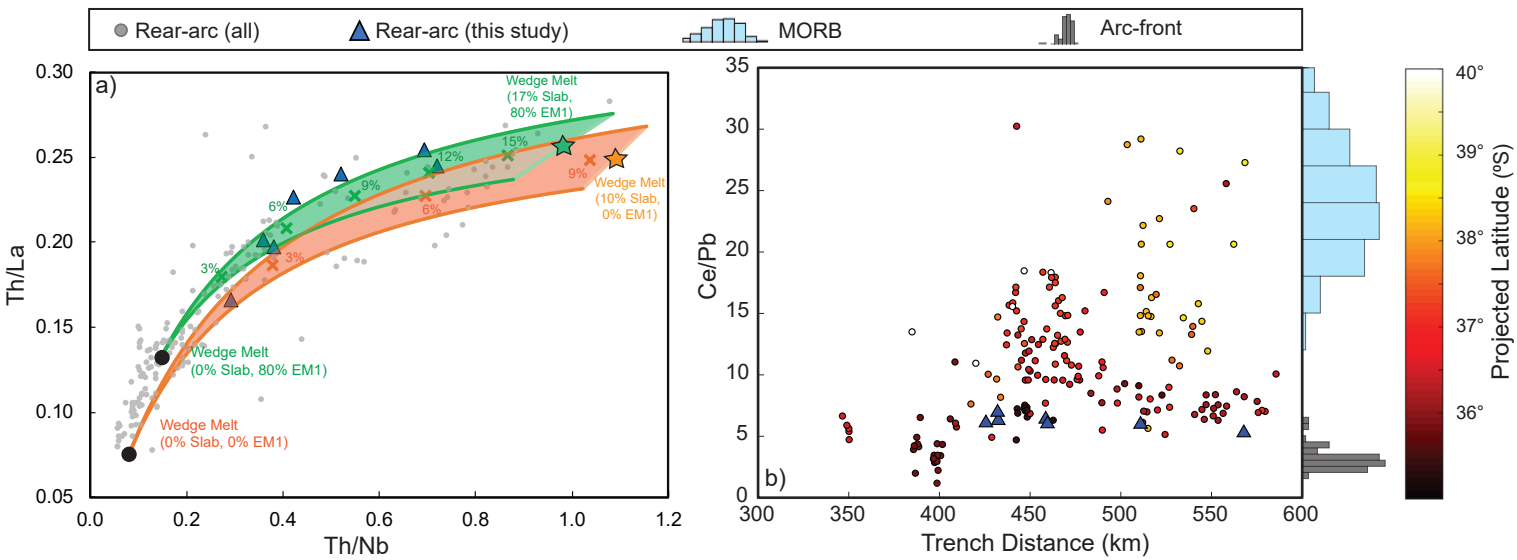
Rear-arc (all)
Rear-arc (this study)
MORB
Arc-front
a)
Th/La
Th/Nb
Wedge Melt (17% Slab, 80% EM1)
Wedge Melt (10% Slab, 0% EM1)
Wedge Melt (0% Slab, 80% EM1)
Wedge Melt (0% Slab, 0% EM1)
3%
6%
9%
12%
15%
b)
Ce/Pb
Trench Distance (km)
Projected Latitude (°S)

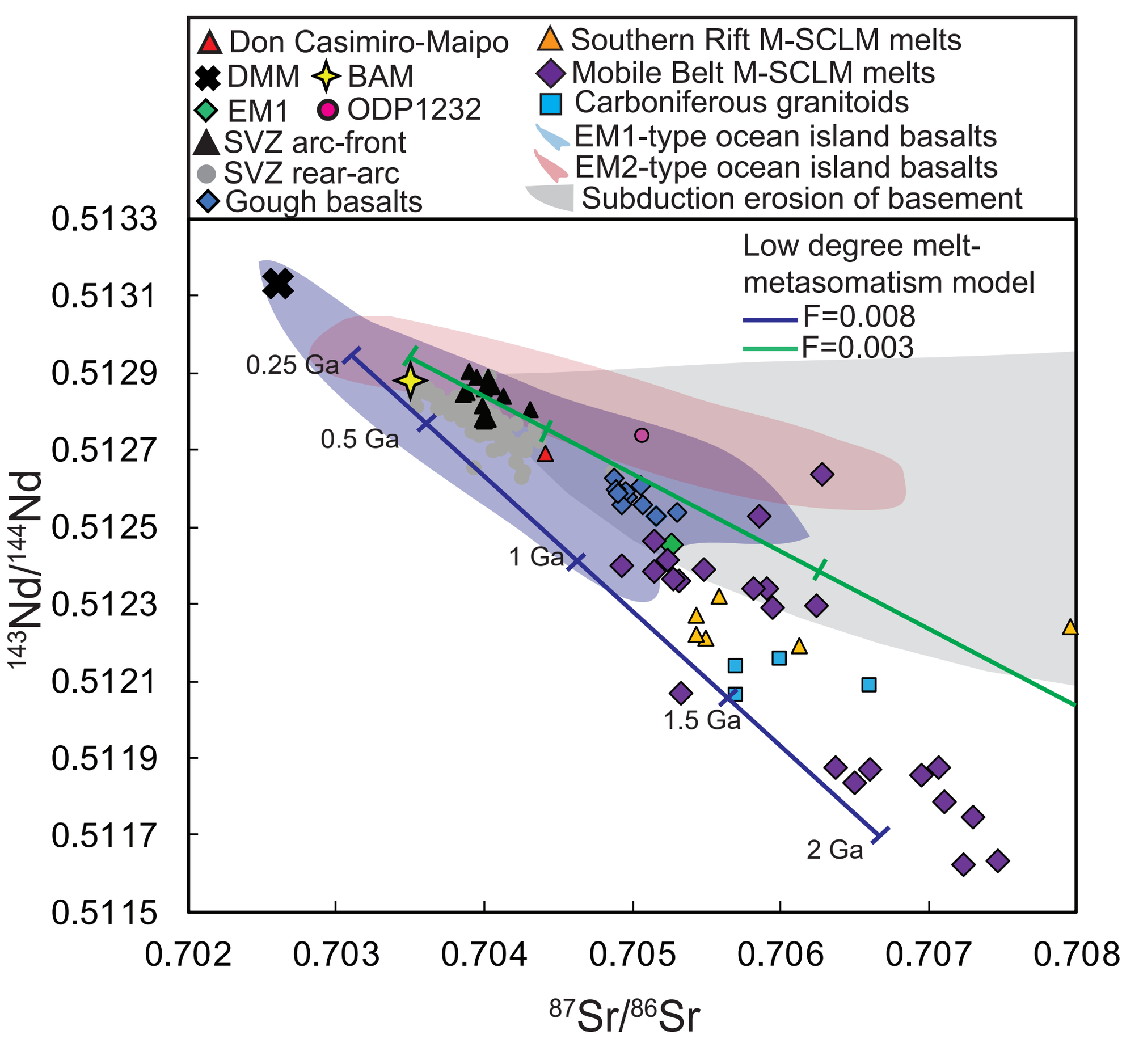
Don Casimiro-Maipo
DMM
BAM
EM1
ODP1232
SVZ arc-front
SVZ rear-arc
Gough basalts
Southern Rift M-SCLM melts
Mobile Belt M-SCLM melts
Carboniferous granitoids
EM1-type ocean island basalts
EM2-type ocean island basalts
Subduction erosion of basement
Low degree melt-metasomatism model
F=0.008
F=0.003
0.25 Ga
0.5 Ga
1 Ga
1.5 Ga
2 Ga
0.5133
0.5131
0.5129
0.5127
0.5125
0.5123
0.5121
0.5119
0.5117
0.5115
143Nd/144Nd
0.702
0.703
0.704
0.705
0.706
0.707
0.708
87Sr/86Sr

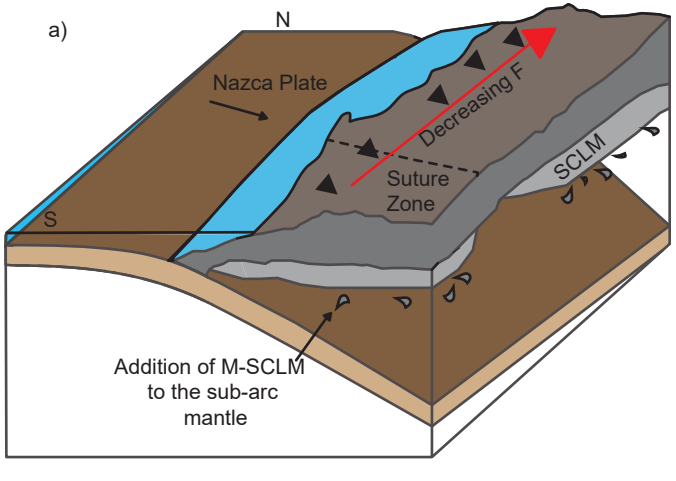
a)
N
Nazca Plate
Decreasing F
Suture
Zone
SCLM
S
Addition of M-SCLM
to the sub-arc
mantle

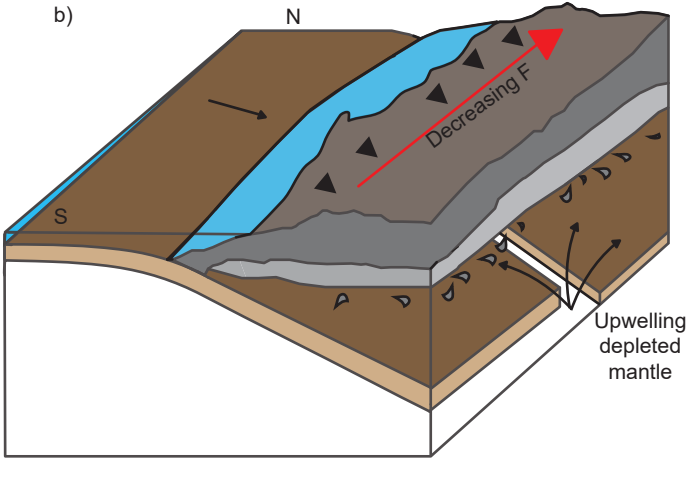
b)
N
Decreasing F
S
Upwelling
depleted
mantle

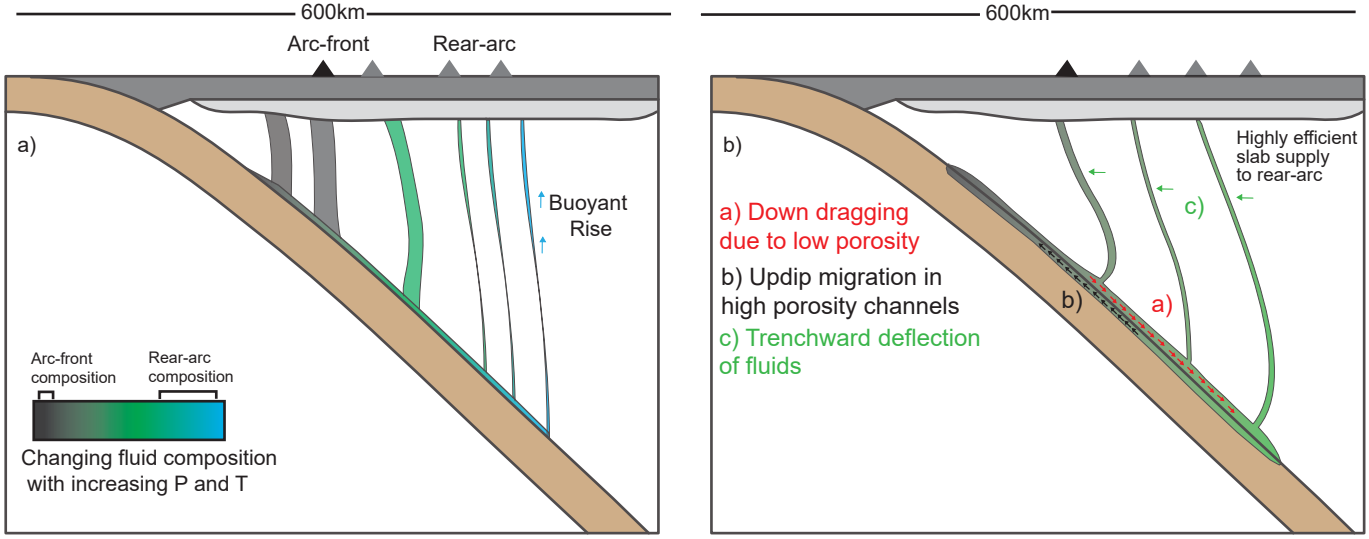
600km
Arc-front
Rear-arc
a)
Buoyant
Rise
Arc-front
composition
Rear-arc
composition
Changing fluid composition
with increasing P and T
600km
b)
Highly efficient
slab supply
to rear-arc
a) Down dragging
due to low porosity
b) Updip migration in
high porosity channels
c) Trenchward deflection
of fluids
c)
b)
a)

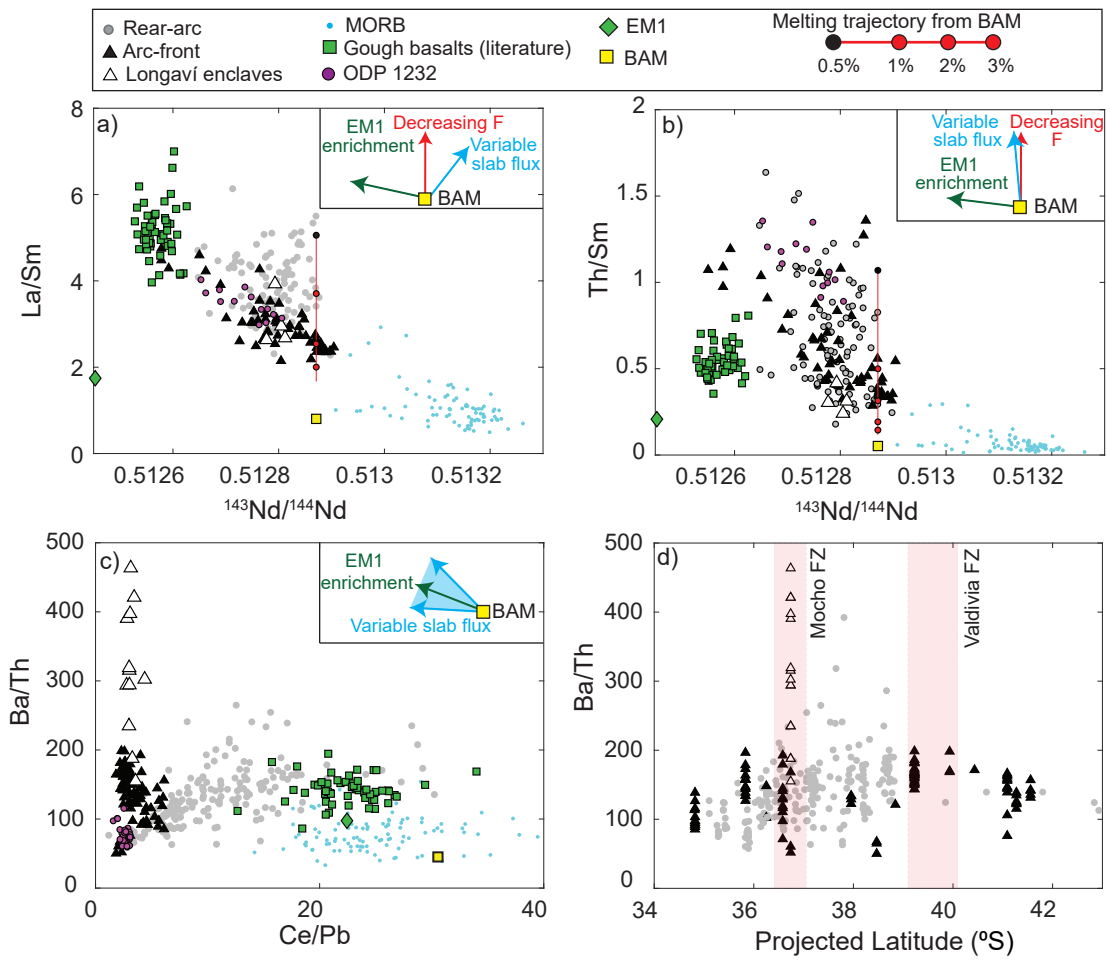
Rear-arc
Arc-front
Longaví enclaves
MORB
Gough basalts (literature)
ODP 1232
EM1
BAM
Melting trajectory from BAM
0.5%
1%
2%
3%
a)
EM1 enrichment
Decreasing F
Variable slab flux
BAM
La/Sm
143Nd/144Nd
b)
Variable slab flux
Decreasing F
EM1 enrichment
BAM
Th/Sm
143Nd/144Nd
c)
EM1 enrichment
BAM
Variable slab flux
Ba/Th
Ce/Pb
d)
Mocho FZ
Valdivia FZ
Ba/Th
Projected Latitude (ºS)

Appendix A: Methods and Sample Details

SIA1 Data and Databases

Whole-rock and olivine analysis from this study is shown in Appendix 3. Compiled rear-arc and Diamante-Maipo literature data used in this study is in Appendix 4. The compilation of SVZ basement compositions is in Appendix 5.

SIA2 Sample Characteristics

Six 100μm sections were made for Don Casimiro-Maipo samples spanning a range of MgO contents. These were scanned using a 5MP slide scanner. Point counting was conducted in JMicroVision by overlaying a 1000 point grid on these scans. Microscope observations were made on any crystals that couldn't be identified with certainty in scans. Crystals smaller than ~0.05mm were classified as matrix. Amorphous or crystalline material sufficiently distinct from the surrounding matrix that could not be identified as a mineral phase was classified as alteration.

Table SA1: Point counting results for Don Casimiro-Maipo samples (ordered by decreasing wt% MgO).

Sample	MgO (wt%)	Crystals (%)	Matrix (%)	Vesicles (%)	Alteration (%)
G0020315-1	6.82	11	89	0	0.1
G0020315-2	6.73	10	90	0	0.3
G0270215-1D	5.63	17	81	0	0.3
G0270215-1C	4.85	14	85	0	0.2
G0030315-4	3.87	11	72	16	0.0
G0030315-1	2.99	42	48	0	10

Table SA2: Percentage of each phenocryst phase in the crystal fraction. *The fine grained nature of these samples meant that phenocryst phases were harder to identify, so proportions are not as reliable as for other samples.

Sample	Olivine (%)	Clinopyroxene (%)	Plagioclase (%)	Oxide (%)	Orthopyroxene (%)
G0020315-1	66	34	0	0	0
G0020315-2	66	34	0	0	0
G0270215-1D*	6	15	46	33	0
G0270215-1C*	8	20	32	41	0
G0030315-4	7	5	89	0	0
G0030315-1	3	13	82	0	3

Table SA3: Description of Don Casimiro-Maipo samples in thin section.

Sample	Olivine	Plagioclase	Clinopyroxene	Matrix Textures
G0020315-1	Predominantly subhedral-anhedral 2-0.5mm grains, and smaller, <0.5mm anhedral grains. Both types form clots, and show association with clinopyroxene. Most olivines contain oxide inclusions.	No phenocrysts.	Subhedral-anhedral 2-0.5mm grains, often forming clots. Smaller, <0.5mm anhedral grains within the matrix. Some show breakdown in their cores.	Dark, fine grained matrix with white streaks of amorphous material. Needle-shaped matrix plagioclase aligns with these streaks. A few 1-2mm patches of alteration are associated with reacted olivine cores.
G0020315-2	Euhedral 1-3mm grains, subhedral 0.5-2mm clots associated with clinopyroxene, and smaller isolated <1mm anhedral grains.	No phenocrysts.	Subhedral 1-2mm grains, often associated with olivine clots. As above, some show broken down cores.	Dark, fine grained matrix, with white amorphous material in streaks. Small needle-shaped plagioclase shows alignment around large crystals. Abundant anhedral oxide grains.
G0270215-1D	Anhedral <0.2mm grains with abraded edges. These are associated with patches of small red amorphous material.	Blocky to needle-shaped plagioclase. No alignment.	Sub-anhedral, 0.3-1mm grains. These are more commonly associated with the red material than olivines.	Dark, fine grained matrix, with poorly aligned, needle-shaped plagioclase, and dispersed anhedral oxides. Patches of white, amorphous material.
G0270215-1C	Anhedral, <0.1mm grains.	Elongated needles, 20:1 aspect ratio. Aligned in matrix.	Sub-anhedral 0.3-1mm grains, associated with red amorphous material and oxide growth.	Dominated by small, aligned, needle-shaped plagioclase, with euhedral-anhedral opaque oxides.
G0030315-4	Anhedral, <1mm grains, with highly abraded edges, likely these were originally clots.	Large, 2mm+, blocky plagioclase, showing sieve textured cores (indicating rapid growth/cooling/heating).	Euhedral, 2-4mm grains, and smaller, <1mm highly abraded anhedral grains.	Highly vesicular texture. Matrix dominated by glass.
G0030315-1	A few subhedral, 1-2mm olivines. Some associated with large, 1-2mm cubic oxide phases.	Several populations of plagioclase. 1) blocky 2-4mm rectangular macrocrysts, with large fluid inclusions. 2) lath shaped 1-3mm grains, with inclusion-free cores. 3) needle shaped (<1mm) grains, with sieve textured cores.	Euhedral-subhedral, 1-2mm grains with oxide inclusions. Some are also associated with very large, 1-3mm oxide grains. Additionally, one 4mm clot of several grains and oxides is observed. In some places, clinopyroxene forms anhedral intergrowths with plagioclase, and orthopyroxene.	Extremely crystal-rich. Large areas of amorphous material within the slide are associated with large blocky plagioclase macrocrysts. Between phenocrysts, the matrix is dark and amorphous.

SIA3 Methodologies

SIA3.1 Whole Rock Chemistry

Sixteen samples from Don Casimiro-Maipo and seven rear-arc samples were prepared for whole-rock analysis at the University of Oxford. Arc-front lava samples were cleaned in an ultrasonic bath until the water ran clear. These were then split into 2-3cm chunks using a pneumatic rock splitter. Rear-arc samples were wet sieved, and unaltered clasts from the coarsest fraction (>2mm) were hand picked for whole rock analysis. Both sample types were crushed in a steel jaw crusher, and then powdered in an agate ball mill.

Major Element Analysis: Major element analyses was conducted by using a PANalytical Axios Advanced X-ray fluorescence spectrometer at the University of Leicester, UK, following the methods of Knott et al. (2016).

Trace Element Analysis: ∼ 100 mg of each powder as well as reference materials BCR-2a, BHVO-2, W-2a and AGV-2, were digested in ∼4ml of 7.5M HNO_3 and ∼1ml of 24M HF. The samples where then evaporated and redissolved twice in ∼4ml 7.5M HNO_3 to eradicate fluoride precipitates. At this stage, a sample split was made for isotopic analysis. Trace element analyses were conducted using a Perkin Elmer NexION 350D quadrupole ICP-MS for the majority of elements. An additional 1200x dilution and addition of an internal standard containing Rh, Re, and In was achieved using the ESI prepFAST system producing a 6000x solution in which to measure lower concentration elements. All prior dilutions were performed gravimetrically. Sample G0030315-4 was run every four samples, and the entire run was duplicated in reverse order to monitor drift. Drift correction and data reduction were carried out following Turner et al. (2013). Due to malfunctioning of the Prepfast system, a planned run at 60,000x dilution for higher concentration elements using the same method failed. Thus, Sr and Ba concentrations were measured using a Thermo Element 2 ICP-MS (also at the University of Oxford) at a 1,200,000x dilution (performed gravimetrically).

The digestion procedure, and sample homogeneity can be assessed by calculating the % difference between the measured element concentrations of two duplicates produced from the powders of this study, and two from an additional set of samples digested alongside these. Most measurements lie within 5%, suggesting that the digestion process, and samples, were reasonably homogeneous (table SA4).

Isotopic Analysis

Strontium (Sr) and neodymium (Nd) isotope analyses were performed on a Thermo Scientific Triton-series multicollector mass spectrometer at the School of Earth and Environment, University of Leeds. Eleven whole-rock powders were digested alongside those for trace element analysis, followed by subsequent drying and pick up in concentrated ultrapure HNO_3 and HCl acids. The final dried samples were diluted and centrifuged for 15 minutes at 2000 rpm. Sr and Nd were extracted by using Sr-Spec and TRU-spec resins and conventional ion-exchange chromatographic techniques. $^{87}Sr/^{86}Sr$ and $^{143}Nd/^{144}Nd$ ratios were normalized for mass fractionation to $^{86}Sr/^{88}Sr$=0.1194 and $^{146}Nd/^{144}Nd$=0.7219. Samples for Sr were loaded onto previously outgassed W filaments and samples for Nd were loaded onto previously outgassed Re filaments. Sr and Nd were analysed while the current was maintained between 3-5 V (for ^{88}Sr) and 0.4-0.8 V (for ^{144}Nd).

The average $^{87}Sr/^{86}Sr$ obtained from repeated measurements of NIST SRM-987 during the course of this study was 0.710271. Similarly, we measured $^{143}Nd/^{144}Nd$=0.511837 for the LaJolla standard. Two samples (G0020315-2 and G0270215-1C) were analyzed for $^{143}Nd/^{144}Nd$ in a separate run, in which we measured $^{143}Nd/^{144}Nd$=0.511850 for the LaJolla standard. We also successfully reproduced the published USGS standard BHVO-2 values for $^{87}Sr/^{86}Sr$=0.703468 and $^{143}Nd/^{144}Nd$=0.512995 (Weis et al., 2005). Details on the sample preparation and analytical protocols are described in Crummy et al. (2014).

SIA3.2 Correction of Isotopic data of this study and Literature Data

Sr and Nd isotopes from the literature and this study were corrected to be in line with the analytical procedure used for SVZ data presented in Turner et al. (2016). Various standards were corrected to be equivalent to La Jolla=0.511858, NBS 987=0.710235 based on session averages.

Table SA4: % deviation of four duplicates ran during analysis on the "quad" (except starred elements, where % deviation is reported from the "element"). (4) represents a duplicate of G0030315-4, (1) represents a duplicate of MDZ1, 079a and B1 are samples measured in the same run, but for use in a study on the Main Ethiopian Rift. % deviation is defined as (Measurement 1-Measurement 2)/(Average of measurement 1 and 2) x 100.

	% difference (4)	% difference (1)	% difference (079)	% difference (B1)
Li	4.13	1.74	-0.97	0.35
Be	-4.52	60.2	-12.4	1.29
Sc	5.89	-27.0	-20.5	-0.72
V	2.02	-1.95	-0.65	0.15
Cr	3.02	0.41	1.14	-0.99
Ni	3.53	0.74	0.86	1.47
Cu	4.71	-3.94	-0.26	1.76
Rb	3.64	0.28	-9.66	0.30
Sr*	5.54	1.74	0.35	-5.67
Y	2.99	-3.08	-6.18	-0.94
Zr	2.12	-0.29	-0.42	0.32
Nb	3.09	0.21	-0.30	1.16
Cs	8.90	-5.49	-4.43	9.11
Ba*	6.08	3.17	3.65	-2.89
La	3.52	0.58	1.10	0.82
Ce	3.31	-1.09	0.94	0.70
Pr	4.57	0.71	2.05	0.80
Nd	3.29	3.63	-0.88	-0.53
Sm	0.00	2.17	1.35	2.23
Eu	2.21	2.20	1.55	-1.12
Gd	3.09	-2.92	-2.87	1.04
Tb	3.26	-2.17	2.29	0.91
Dy	3.83	-0.60	2.67	0.78
Ho	4.64	-2.73	-0.32	3.88
Er	2.99	4.01	-2.53	3.70
Tm	2.81	-5.67	-3.75	0.51
Yb	2.67	1.49	-0.23	1.69
Lu	1.28	1.41	-3.58	1.15
Hf	3.34	0.93	-0.87	1.40
Ta	-2.98	-0.57	1.60	-0.94
Pb	3.55	-2.14	-9.60	1.72
Th	3.48	-2.05	-17.6	-1.10
U	3.33	-0.09	0.56	-0.11

SIA3.3 Olivine Chemistry

Olivines were picked from the 1000-250μm grain fractions, and mounted in epoxy rings. These mounts were polished and carbon coated for EMPA analysis. Analysis was conducted with an accelerating voltage of 15KeV, a current of 100nA and a 10μm spot size. St John's Island and Fayalite were run as secondary standards, with % recoveries reported in table SA5.

LA-ICP-MS analysis was conducted at the University of Cambridge. Three instrument runs were performed over two days. The run conditions were 20Hz, 80µm, 9.5J/cm^2, 0.8L/min of gas flow for He and Ar. Where possible, three spots were placed in the centre of the olivine, with no overlap. For very small grains, only 2 spots were placed, as it is preferable to have fewer spots nearer the centre than more spots towards the grain edges, due to the reasonably high diffusivity of elements of interest to this study. To allow drift correction, 3 spots on each of

NISTSRM612, NISTSRM610, 06SGOL03 (inhouse olivine standard) and BD4074OL-7 (a San Carlos olivine) were run every 30 analyses. ^{29}Si was used as an internal standard, with values obtained from EMPA grain averages. Signals were selected using Glitter Processing software, with normalization to NISTSRM612 via a quadratic drift correction. This was effective at removing drift, as determined by observing the stability of NISTSRM610, 06SGOL03 and BD4074OL-7 following this correction. Multiple secondary standards were run to assess the accuracy of the measurement for elements of interest (NISTSRM610, NISTSRM614, BCR-2G). Measurement of inhouse olivines O6SGOl03 and BD407OL-7 provided an excellent assessment of the success of the drift correction performed on glass standards. Elements of interest in this study drifted by less than 7%. Although Mn and Ni recovery on glass standards were good, these elements were recovered more poorly on BCR-2G. This, and the fact that previous studies in this area have used EMPA Ni and Mn data, resulted in us choosing to use EMPA data for consistency, as most of the peridotite-pyroxenite ratios involve normalization to Fe (which is reported from EMPA). Detection limits, and 1 sigma uncertainties calculated from Glitter for a representative sample (MDZ2) are shown in table SA6.

Table SA5: Peak count times, and calibration materials used. % recovery calculated below is defined as Measured Average/Published Average x 100. Where no published value exists for a standard, - is shown. Detection limits are reported from 9 spots on MDZ8. These are assumed to be representative of the analysis as a whole.

	Mn	Fe	Mg	Si	Ca	Ni
Peak count times (s)	20	30	20	20	70	70
Calibration material	Mn metal	Andradite	MgO	Albite	Wollastonite	Ni metal
% Rec Fayalite	97.7	94.2	-	99.6	97.0	-
% Rec St Johns Island Olivine	106.1	96.1	99.6	99.2	-	90.1
Detection limit (ppm)	173	197	173	98	74	137

Table SA6: Minimum (99% Confidence) detection limits (ppm), and 1 sigma uncertainties (ppm) for all spots on MDZ2, taken as representative for the analysis as a whole. The mass in brackets represents the isotope measured on the ICP-MS.

Element	MDL	1 σ uncertainty
Li(7)	0.115	0.151
Na(23)	1.121	6.92
Al(27)	0.318	39.3
P(31)	13.76	47.3
Ca(43)	133	192
Sc(45)	0.062	0.412
Ti(47)	0.551	18.4
V(51)	0.043	0.504
Cr(53)	0.578	56.0
Mn(55)	0.136	88.4
Co(59)	0.049	7.91
Ni(60)	0.171	191
Cu(65)	0.351	0.416
Zn(66)	0.373	10.1
Ga(69)	0.042	0.049
Ge(72)	0.370	0.208
Y(89)	0.037	0.025
Zr(90)	0.033	0.052
Nb(93)	0.035	0.021

Table SA7: % recovery of NISTSRM610 (average of 3 spots). (x,y) refers to when this secondary standard was run, x referring to the instrument run (1-3), and y to the order of measurement within a given run. These values were used to check the success of the quadratic drift correction. Across the three instrument runs, most elements drift by less than 10%.

Element	(1,1)	(1,2)	(1,3)	(1,4)	(1,5)	(2,1)	(2,2)	(2,3)	(2,4)	(3,1)	(3,2)	(3,3)	(3,4)	AVERAGE
Li(7)	98.0	105.5	103.7	106.7	105.9	107.3	104.3	101.1	103.6	108.0	99.6	96.8	98.2	103.0
Na(23)	98.2	105.7	107.0	106.1	105.9	105.9	104.9	101.4	103.9	105.0	103.0	101.1	102.1	103.9
Al(27)	102.3	105.5	105.9	106.2	107.8	108.3	104.2	104.9	107.3	105.6	107.2	103.5	104.9	105.7
P(31)	107.8	105.2	99.7	130.9	194.5	100.5	103.9	101.0	100.5	125.0	113.1	117.6	133.9	118.0
Ca(43)	95.9	103.7	100.6	106.7	107.3	105.2	102.5	99.2	102.2	105.2	100.1	99.5	104.5	102.5
Sc(45)	98.7	109.1	108.0	109.8	108.8	110.2	110.9	105.6	108.9	108.5	106.7	108.0	109.6	107.9
Ti(47)	115.2	120.8	116.9	120.0	119.0	125.1	128.7	124.5	125.5	125.3	125.9	122.8	125.4	122.7
V(51)	95.7	101.9	100.1	105.2	105.8	104.8	102.6	100.1	105.1	105.9	101.7	99.9	103.7	102.5
Cr(53)	103.4	107.7	109.4	113.6	119.5	120.7	115.9	112.1	115.1	114.1	111.4	112.7	116.7	113.2
Mn(55)	94.6	100.0	100.0	103.7	102.4	105.1	100.2	99.0	103.5	104.9	97.1	96.1	97.7	100.3
Co(59)	95.5	103.0	101.7	103.7	100.8	104.2	102.0	98.9	104.3	103.6	101.0	100.3	103.4	101.7
Ni(60)	92.1	100.9	99.8	103.7	99.9	105.6	100.1	98.2	100.0	104.3	101.8	100.5	102.2	100.7
Cu(65)	89.9	98.8	97.3	100.1	97.5	100.5	98.4	94.9	99.0	100.1	96.0	95.9	97.6	97.4
Zn(66)	98.5	104.1	102.3	108.8	110.2	111.1	104.4	100.1	106.6	109.9	106.4	104.1	102.9	105.3
Ga(69)	92.2	97.7	96.5	101.1	101.5	101.7	99.0	97.2	99.4	101.4	98.9	98.3	100.8	98.9
Ge(72)	81.5	86.7	85.7	89.1	88.8	92.4	89.0	85.6	86.6	92.0	87.5	87.8	89.8	87.9
Y(89)	93.1	102.1	99.8	102.8	102.1	104.0	102.9	100.5	100.3	102.5	101.4	101.8	103.8	101.3
Zr(90)	89.8	95.9	94.6	97.9	98.1	98.6	98.5	94.6	95.4	97.5	96.8	96.0	98.7	96.3
Nb(93)	92.8	99.9	98.9	102.4	101.7	102.2	102.2	98.1	100.2	102.9	99.9	99.2	101.1	100.1

Table SA8: % recovery of BCR-2G, using averages from 3 spots, and % recovery of NISTSRM614. The % recovery for NISTSRM614 is not shown for the first run. These were the first spots ran by the laser, and it has been shown that the system takes a few spots to warm up and settle after switching from solution mode to laser mode.

Element	(1,1)	(2,1)	(2,2)	(3,1)	(3,2)	BCR-2G Average	(2,1)	(3,1)	NISTSRM614 Average
Li(7)	100.2	104.5	101.7	105.8	94.6	101.4	84.4	103.7	94.1
Na(23)	96.2	99.1	97.0	101.4	96.9	98.1	105.5	103.1	104.3
Al(27)	103.8	103.4	99.9	104.6	103.3	103.0	106.6	106.3	106.4
P(31)	101.3	84.9	86.8	108.4	120.1	100.3	268.2	260.0	264.1
Ca(43)	99.0	97.9	98.9	101.1	99.1	99.2	106.2	103.7	105.0
Sc(45)	97.5	102.1	96.4	100.8	99.9	99.3	217.1	185.9	201.5
Ti(47)	107.3	108.4	105.2	110.9	106.3	107.6	122.1	101.3	111.7
V(51)	97.6	100.1	101.1	102.8	99.6	100.2	109.7	99.9	104.8
Cr(53)	93.2	104.4	92.9	97.1	101.1	97.7	94.8	113.0	103.9
Mn(55)	92.4	96.6	94.9	98.5	90.0	94.5	105.6	89.7	97.7
Co(59)	99.0	97.8	97.0	97.9	96.2	97.6	92.6	95.0	93.8
Ni(60)	89.4	86.9	83.8	90.2	86.5	87.4	107.9	71.8	89.8
Cu(65)	71.0	72.5	67.5	71.1	69.6	70.3	88.8	109.0	98.9
Zn(66)	121.5	134.0	127.4	134.9	120.7	127.7	91.4	89.2	90.3
Ga(69)	111.6	117.1	109.2	118.4	114.5	114.2	96.9	93.9	95.4
Ge(72)	99.6	112.9	95.6	101.1	102.4	102.3	86.3	110.8	98.5
Y(89)	87.3	90.0	81.9	90.6	89.1	87.8	102.0	99.4	100.7
Zr(90)	84.5	87.0	78.3	87.7	86.3	84.7	90.3	91.6	90.9
Nb(93)	88.6	91.6	86.6	91.0	90.2	89.6	93.7	99.3	96.5

SIA4 Mantle Melting Model Details

As discussed in the text, this study uses an updated version of the model of Turner and Langmuir (2015b). Below, the justification of various inputs to the model are discussed. The updated Matlab scripts ADD_SLAB.m, ADD_SLAB_HOTP.m and ModeMelt_Hydrous.m have been uploaded into the supplementary information.

SIA4.1 Model Partition Coefficients

Hydrous Partition Coefficients for Mantle Melting: This study utilizes hydrous partition coefficients and mantle modes from Turner and Langmuir (2015b; detail in their supplement). However, we slightly updated the partitioning behaviour of several elements:

1) The bulk partition coefficient of Eu is obtained by a log extrapolation from those of Sm and Gd:

$$\mathrm{Kd}_{Eu} = (\mathrm{Kd}_{Sm}{*}\mathrm{Kd}_{Gd})^{0.5}$$

correcting an error in Turner and Langmuir (2015b).
2) The partition coefficient of Hf is assumed to be equal to that of Sm.
3) The partition coefficient of Zr is approximated as:

$$\mathrm{Kd}_{Zr} = (\mathrm{Kd}_{Nd}{*}\mathrm{Kd}_{Sm})^{0.5}$$

Hydrous Partition Coefficients for slab melting: As above, this study uses slightly adapted partition coefficients for slab melting to those in Turner and Langmuir (2015b). These lie within the limits of experimental values (figure SA1). The partition coefficients for the LREE (La, Ce, Nd, and Sm) were reduced by 40% to reflect the hotter slab underneath Don Casimiro-Maipo (inline with experimental high temperature partitioning results; figure SA1). Additionally, the partition coefficients of Zr and Hf were reduced, and 70% of Cs was assumed to be lost to the forearc.

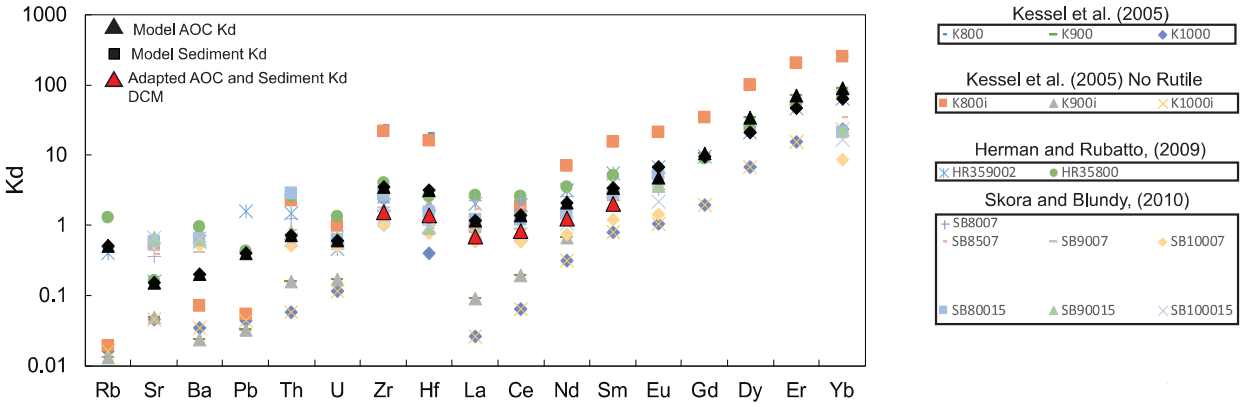

Figure SA1: Slab melting partition coefficients lie within experimental values for 800-1000°C.

SIA4.2 Model End-Members

"Ambient Andean Mantle" (Depleted Mantle End-Member): The isotopic composition of the depleted mantle end member was set to $^{87}Sr/^{86}Sr$=0.70355 and $^{143}Nd/^{144}Nd$=0.512871, the isotopic composition of sample 126171 of Soager et al. (2013) following the isotopic correction discussed above. This sample lies at the depleted end of the rear-arc array, and thus reflects the composition of the Andean mantle prior to the addition of EM1 enrichment. For trace element modelling, the depleted mantle end-member is DMM of Workman and Hart (2005).

AOC: The subducting Nazca plate has Pacific affinities. Trace element concentrations were obtained from melting of N-MORB (Gale et al., 2013) at 876°C, F=0.3. The isotopic composition of AOC was set to $^{87}Sr/^{86}Sr = 0.7035$, $^{143}Nd/^{144}Nd = 0.5130$.

Sediment: The trace element composition of the sediment end-member was obtained from 33 samples of ODP1232 (c.f. Turner et al., 2017). To produce an envelope of model results for trace elements and isotopes, one standard deviation of measured samples were added and subtracted to the mean. Three outliers were discarded based on their anomalously high Sr isotope ratios.

Enriched EM1 end-member: Enrichment at Gough represents a mix of M-SCLM, and ambient mantle. The isotopic signature of recycled M-SCLM depends on the storage time (Turner et al., 2017). As several samples within this study have signatures more enriched than Gough, we use the isotopic composition of a sample from Pitcairn (57DS9; Stracke et al., 2003) as the EM1-like isotopic end member. This lies at the enriched end of the field

enclosing EM1-type ocean island basalts. The trace element concentration was obtained from the inversion of Turner et al. (2017), with a few changes:
1) the bulk Eu partition coefficient was set at:

$$\mathrm{Kd}_{Eu} = (\mathrm{Kd}_{Sm} * \mathrm{Kd}_{Gd})^{0.5}$$

correcting an error in Turner et al. (2017) where it was set at 0.
2) The Zr concentration in Gough primary melts was adjusted to the standard EM1 value Zr/Hf = 45.
3) Zr partition coefficients were extrapolated from Salters and Longhi (1999).
4) Nb and Ta partition coefficients were taken as $\mathrm{Kd}_{La}/3$, based on ratios from Workman and Hart (2005).

Table SA9: Gough mantle source composition used in this study compared to that of Turner et al. (2017; T2017).

	Eu	Zr	Nb	Ta
This study	0.130	6.70	0.403	0.024
T2017	0.0234	11.47	0.472	0.028

SIA5 References

Crummy, J., Savov, I.P, Navarro-Ochoa, C., Morgan, D., Wilson, M., 2014. High-K mafic Plinian eruptions of Volcán de Colima, México, Journal of Petrology, 55 (10). pp.1-18.

Kessel, R., Schmidt, M.W., Ulmer, P. and Pettke, T., 2005. Trace element signature of subduction-zone fluids, melts and supercritical liquids at 120–180 km depth. Nature, 437(7059), pp.724-727.

Knott, T.R., Branney, M.J., Reichow, M.K., Finn, D.R., Coe, R.S., Storey, M., Barfod, D. and McCurry, M., 2016. Mid-Miocene record of large-scale Snake River–type explosive volcanism and associated subsidence on the Yellowstone hotspot track: The Cassia Formation of Idaho, USA. Bulletin, 128(7-8), pp.1121-1146.

Roduit, N. JMicroVision: Image analysis toolbox for measuring and quantifying components of high-definition images. http://www.jmicrovision.com (accessed 4th January 2017).

Salters, V. and Longhi, J. (1999). Trace element partitioning during the initial stages of melting beneath mid-ocean ridges. Earth and Planetary Science Letters 166: 15-30. doi: 10.1016/S0012-821X(98)00271-4.

Turner, S.J., Izbekov, P. and Langmuir, C., 2013. The magma plumbing system of Bezymianny Volcano: Insights from a 54 year time series of trace element whole-rock geochemistry and amphibole compositions. Journal of Volcanology and Geothermal Research, 263, pp.108-121.

Weis, D., Kieffer, B., Maerschalk, C., Pretorius, W., Barling, J. 2005. High-precision Pb-Sr-Nd-Hf isotopic characterization of USGS BHVO-1 and BHVO-2 reference materials. Geochemistry Geophysics Geosystems, 6, Q02002.

Appendix B

SIB1 Evidence for AFC processing

As mentioned briefly in the main text, when samples from the entire Diamante-Maipo caldera complex are considered, the correlations between $^{87}Sr/^{86}Sr$ and $^{143}Nd/^{144}Nd$ and indices for fractionation and assimilation (MgO and Eu/Eu*) provide strong evidence for AFC (figure SB1)

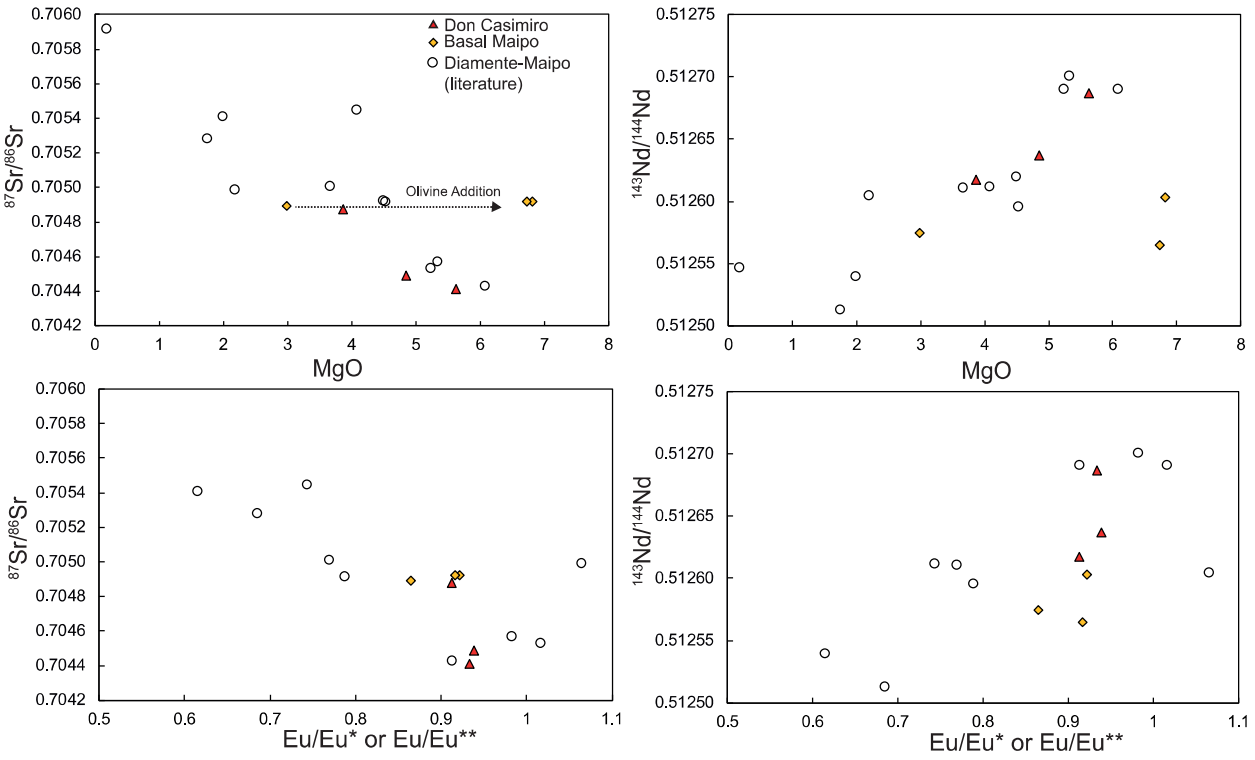

Figure SB1: Within the Diamante-Maipo Caldera, isotopic enrichment increases with assimilation and fractionation. The signal of olivine addition for the two most primitive Maipo samples is also clear.

SIB2 Evidence for Olivine Addition

EMPA analysis indicates that Don Casimiro-Maipo olivines lie significantly below the olivine-whole rock equilibrium line (Figure SB2a), indicating excess olivine accumulation. The two most primitive samples, which are from the basal section of Maipo volcano, can be related to the otherwise coherent liquid line of descent among the Diamante Caldera samples by the addition of 7 wt. % Fo 81 olivine (figure SB2b-d.). All samples have phenocrysts of olivine and clinopyroxene, so this trend is not consistent with fractionation of these two phases together. Olivine may have been accumulated from a mush pile produced by fractionation before clinopyroxene appears on the liquidus. This serves as an excellent example of the importance of utilizing individual mineral analyses in conjunction with whole-rock data when interpreting subtle geochemical variations within individual volcanic groups. While it is tempting to represent the parental composition of a volcanic group using the most

olivine-phyric samples (6-7vol% olivine, in this case), such samples can often have more complicated petrogenetic histories.

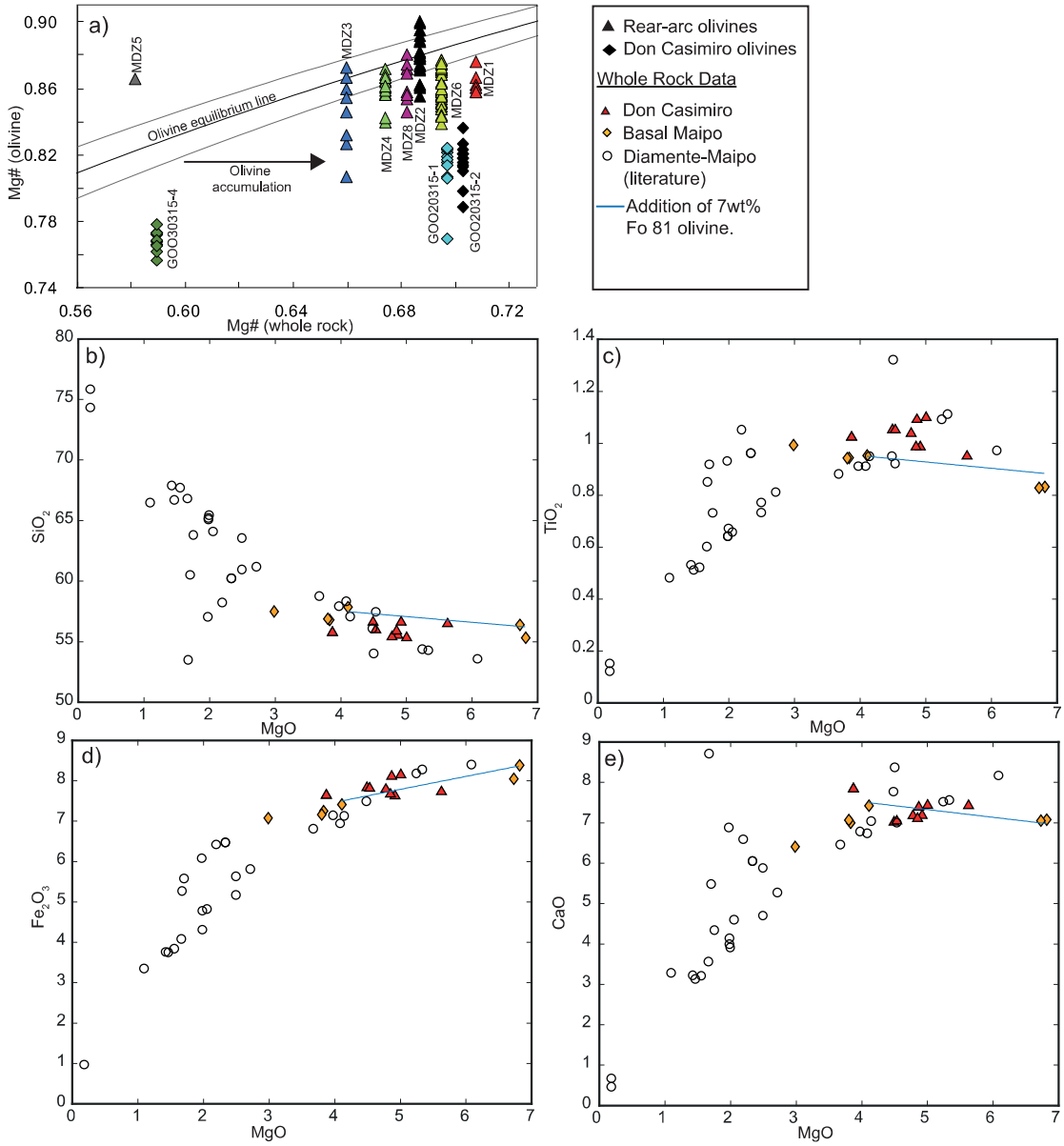

Figure SB2: a) Don Casimiro-Maipo samples show strong evidence for olivine addition, with olivine compositions plotting below an equilibrium line calculated using Roeder and Emslie (1970), Kd=0.3±0.03, assuming whole-rock Fe^{3+}/Fe_T=0.3 (Holm et al., 2016). Most rear-arc olivines plot near to or below the equilibrium line, suggesting minor olivine addition (assuming whole-rock Fe^{3+}/Fe_T=0.15, Søager et al., 2015b). b-d) Addition of 7 wt% Fo 81 olivine from more evolved Maipo samples produces a good match to the most primitive samples, showing that their high MgO contents are spurious. Diamante-Maipo whole-rock data literature data used in this study is from Hickey et al. (1986), Futa and Stern, (1988), Sruoga et al. (2005), Holm et al. (2014) and Hickey et al. (2016).

SIB3 Changes in Slab Conditions Inferred from Zr-Hf Anomalies

Using Hf/Sm as a proxy, we find that rear-arc and most arc-front volcanics have a similar range of Zr-Hf values, but Don Casimiro-Maipo has a less pronounced Zr-Hf anomaly (figure SB3). The smaller Hf/Sm (and thus Zr-Hf anomaly) at Don Casimiro-Maipo may reflect the fact that the slab is slightly hotter, which causes residual slab zircon to become more soluble in the slab melt (Hirai et al., 2018).

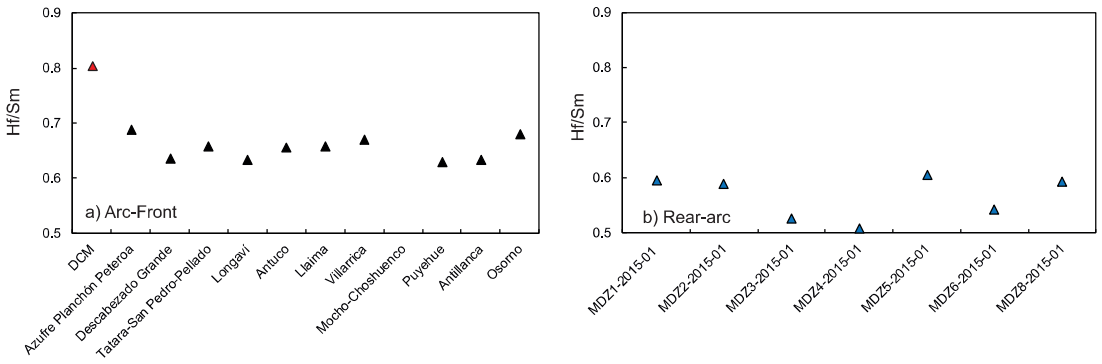

Figure SB3: a) Don Casimiro-Maipo has a significantly different Hf/Sm signature to the rest of the SVZ (data for other centers from Turner et al., 2016). b) Rear-arc centers of this study have similar Hf/Sm ratios to the SVZ arc-front as a whole.

SIB4 Assessing the evidence for LCC assimilation in the SVZ rear-arc

As discussed in section 4.5 of the main text, the offset trajectories of rear-arc and arc-front lavas in trace element and isotope space have been explained by various regional models. We show that these offsets can instead be accounted for a model incorporating variable amounts of EM1 enrichment, combined with variable slab fluxes and melt extents (figure 13 of the main text). This three-parameter model can also account for the offset trajectories in Nd-Hf isotope space (figure SB4). Arc-front and rear-arc lavas both spread along a mixing line between depleted and enriched mantle sources. Arc-front lavas are shifted to the right of the trajectory defined by rear-arc samples due to higher slab fluxes. Additionally, while rear-arc lavas appear to trend towards the composition of LCC xenoliths (Kay et al., 1996) in Ba/Th vs U or Ce/Pb space, calculated mixing lines are hyperbolic, and do not reproduce the trajectory of the rear-arc array (Figure SB5). To accommodate the mis-match between the LCC xenolith mixing model and the rear-arc data, Soager et al. (2013) instead adapt a model LCC composition that has been adjusted for several elements. These adjustments, however, diverge substantially from both global models of the LCC composition as well as the compositional field defined by the larger compilation of Andean basement lithologies (figure SB6).

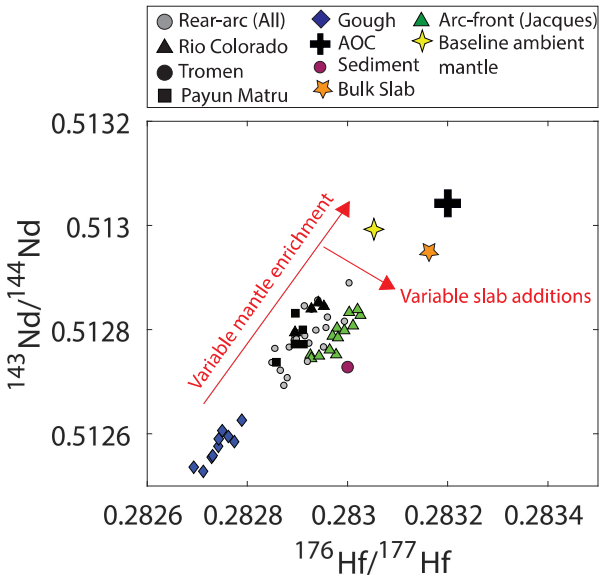

Figure SB4: The offset trends of rear-arc and arc-front lavas in Hf-Nd isotope space can be accounted for a unified model with variable EM1-type enrichment combined with variable slab inputs (see Turner et al., 2017).

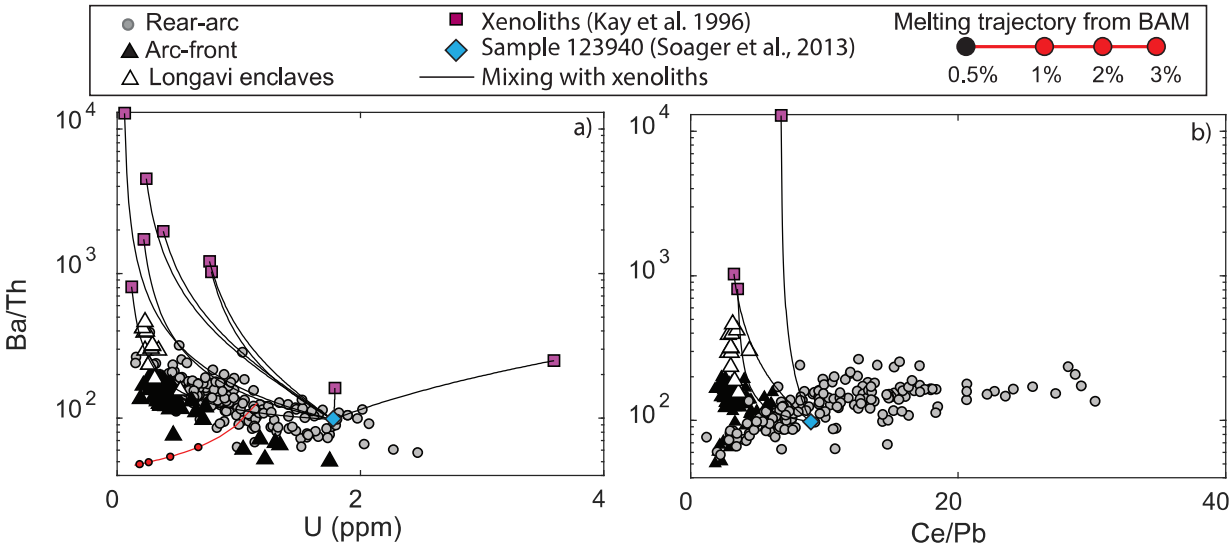

Figure SB5: Soager et al. (2013) suggest that the trajectory of rear-arc lavas trend towards the composition of xenoliths sampled by Kay et al. (1996) in Ba/Th vs. U and Ce/Pb space. However, calculated mixing trajectories between sample 123940 (used in the modelling of Soager et al., 2013) and these xenoliths fail to recreate the rear-arc trends on both plots.

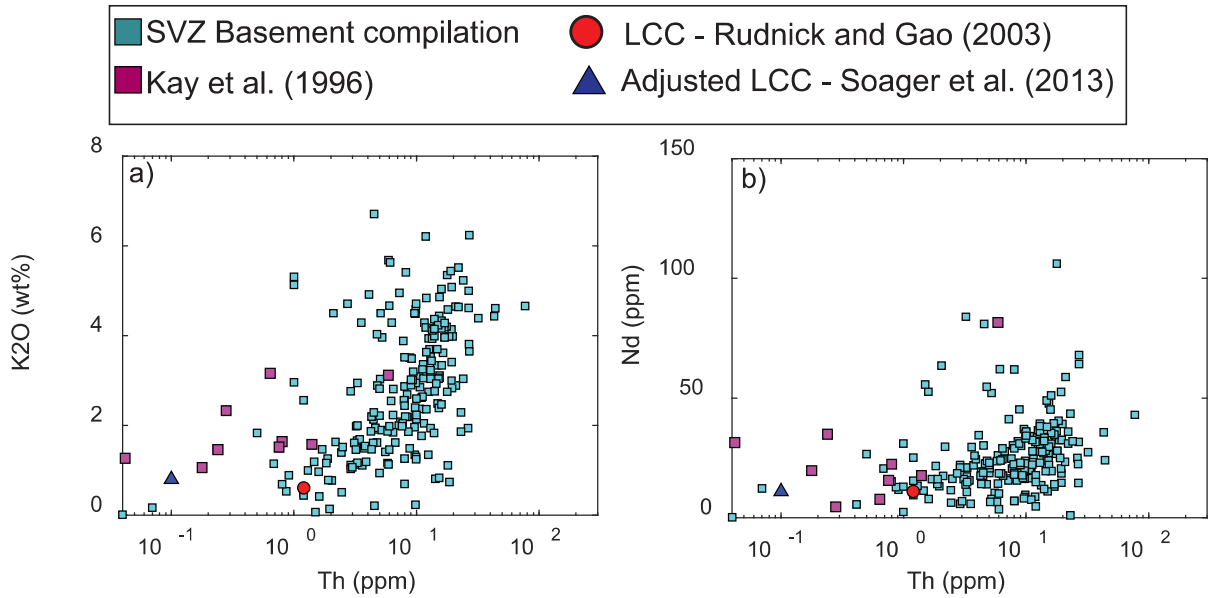

Figure SB6: Comparison of SVZ basement compositions (cyan squares) to the composition of the xenoliths of Kay et al., (1996), the LCC (Rudnick and Gao, 2003), and the basement composition used in the modelling of Soager et al. (2013). It is clear that neither the xenoliths nor the LCC composition of Rudnick and Gao (2003) is particularly representative of the composition of SVZ basement lithologies. Given that the LCC composition of Rudnick and Gao (2003) already deviates substantially from observed SVZ basement lithologies, the adjustments made to the global LCC composition by Soager et al. (2013) are difficult to justify.

References

Roeder, P.L. and Emslie, R., 1970. Olivine-liquid equilibrium. Contributions to mineralogy and petrology, 29(4), pp.275-289.